Engineering Structures 183 (2019) 160–179

Contents lists available at ScienceDirect

Engineering Structures

journal homepage: www.elsevier.com/locate/engstruct

Seismic control of modularized suspended structures with optimal vertical distributions of the secondary structure parameters

Zhihang Ye, De-Cheng Feng, Gang Wu*

Southeast University, Key Laboratory of Concrete and Prestressed Concrete Structures of the Ministry of Education, Nanjing 210096, China

ARTICLE INFO

Keywords:
Suspended structure
Mega-substructure system
Modular construction
Vertical irregularity
Passive vibration control
Multi-objective genetic algorithm

ABSTRACT

Suspended building systems with vibration control features dissipate seismic energy by the interaction between their main parts and the suspended parts; they are also architecturally appealing. A modularized suspended structure has been previously proposed to overcome the fragility of its secondary structure and to enhance overall attenuation. However, the full potential of modularization is yet to be achieved via the previous configuration, especially in terms of multi-mode control. In this study, the protection effect of prefabricated modules is further harnessed in such a way that drastic vertical-irregularities of inter-story stiffness and dampers within the suspended segment are allowed. Vertical distribution vectors of structural parameters were set as the variables in genetic-algorithm optimizations, with the maximum mean square moment of the primary structure being the main objective. The results show considerably improved attenuation of responses in multiple modes instead of only the fundamental mode. In the optimized distributions, peaks of damping coefficient occur at the troughs of inter-story stiffness, but without a highly concentrated pattern. Models with different irregularity levels have well-separated Pareto fronts; this indicates that comprehensive improvement can be obtained at compromised choices. The main mechanism is that, with the well-designed irregularities, the secondary structure provides satisfactory dissipation and tuning to the primary structure in the major modes. The analysis with non-stationary excitations reveals that optimized vertical distributions further quicken the vibration decay. The time-history performance verifications and the structural uncertainty analysis are also carried out.

1. Introduction

Mega-substructure systems [1–14] consist of two structural parts, namely, the main part (the primary structure) and the suspended or base-isolated part (the secondary structure) which is architecturally functioning. Various forms of mega-substructure systems exist: core-tube with suspended floors [1,2,7,8,14], mega-frame with suspended floors [5] or isolated floors [3,6,12], frame structure with suspended floors [10] or isolated floors [11], isolated roof [4] and inter-story isolations [9,13]. While the secondary structure delivers loads to the primary structure, the relative motion between the two parts can be harnessed to dissipate energy and reduce vibration. Mega-substructure systems possess high robustness [3,15] against parameter deviation and wide-band excitations in terms of passive vibration control and can be applied to scenarios in which regular dampers cannot perform with the highest efficiency [3]; these scenarios include systems with dominant flexural-type deformation such as core-tubes. In this kind of systems, the secondary structures interact with the primary structure over a wide frequency range, with the secondary structures being large-scale tuning masses, energy absorbers as well as spaces with attenuated accelerations. A majority of suspended building structures [1,2,5,7,8,14] belong to the category of mega-substructure systems and are architecturally appealing as the vertical members are tensioned instead of compressed, leading to reduced cross sections and, consequently, increased transparency along with reduced weights [1,8]. Additionally, a large column-free space can be easily formed in the first story [16].

If a flexible suspended segment is directly connected to the primary structure [1,5,17], the relative motion is developed through deformation within the suspended segment. However, non-structural members within multi-story suspended segments are susceptible to inter-story drift, for which a limit is therefore set far lower than which is required by the primary-structure-oriented optimum [14]. This issue also undermines the attenuation of acceleration within the secondary structure and may be worsened if a glazed curtain wall is adopted to emphasize the aforementioned architectural merits [18]. The authors have previously proposed a subtype of suspended building structures that harnesses the protection effect of the suspended discrete modules [14], which are 3D prefabricated units [19–22], to overcome this fragility. In

* Corresponding author.
E-mail address: g.wu@seu.edu.cn (G. Wu).

https://doi.org/10.1016/j.engstruct.2018.12.099
Received 1 June 2018; Received in revised form 20 November 2018; Accepted 30 December 2018

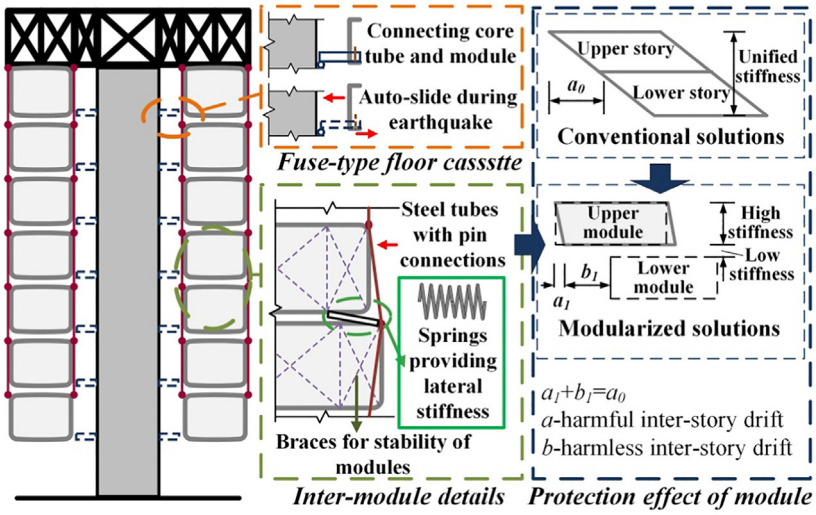

(a) Diagram of previously proposed modularized suspended structure

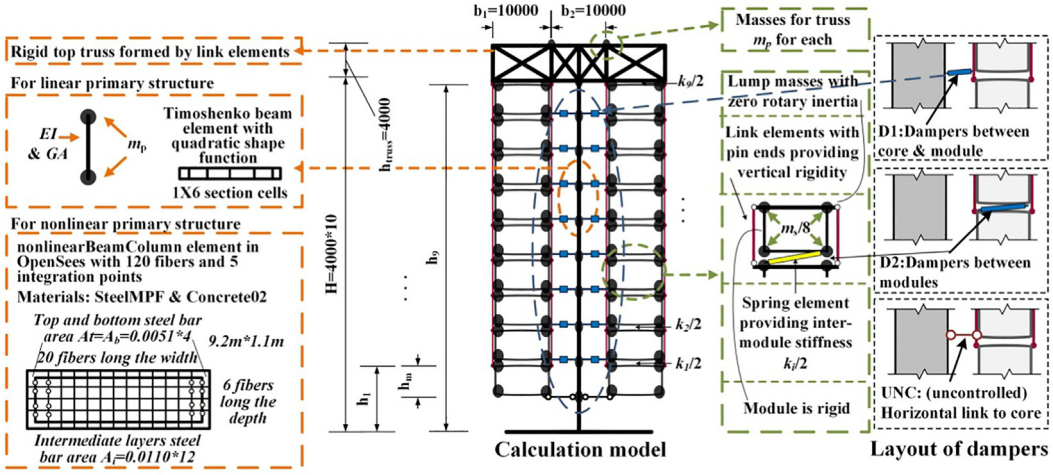

(b) Calculation model

Fig. 1. Diagram of modularized suspended structure and calculation model.

this previous work, a satisfactory improvement in overall control performance is achieved by sufficient relative motion, tuning between a higher mode of the secondary structure and the first mode of the primary structure, and a wider and deeper trough of the primary structure. The limitation is the small number of optimizing variables, the mechanism focusing on dynamic features only in low-frequency range, and the un-tuned higher mode of the primary structure. Thus, the full potential is yet to be achieved.

As for multi-mode control, previous studies [23] used a combinatorial optimization method to distribute viscous dampers in shear buildings given limited number of dampers, with the resulting power spectral density functions showing multi-mode vibration reduction. Previous studies [24] showed that the optimized vertically distributed multiple tuned mass dampers are able to suppress the vibration response of a shear-building in multiple modes and outperform the single-TMD in terms of peak time-history response. Comparatively, single-TMD may increase higher-mode response when tuned to the fundamental mode, and it is not beneficial in response to impulse-type ground motions. Previous studies [25] pointed out that a body-type TMD has the potential to tune 6 of the structure modes. The minimal damping in a frequency range was maximized for a structure-MDOF TMD system. In the free-free beam case, an MDOF TMD can be designed to provide higher damping in the first three modes, when compared with multiple SDOF TMDs.

The suspended structure can be treated as a structure-MDOF TMD system with vertically distributed viscous dampers, but the suspended segment is heavy, functioning and fragile, with multiple connections to the core, as compared with traditional TMDs. As a result, in order to facilitate dissipation in several frequency ranges where the primary structure responses are considerable, it will be presumably necessary for the system to have precisely distributed modes with desirable shapes, under the strong influence of the suspended segment. That is an intrinsic difference from the cases in the aforementioned studies.

For modularized suspended structures, the three following questions are worth investigating: 1. In frequency domain, desirable modal frequency spacing can evade the dominant content of the excitation, and the desirable complex mode shapes indicate good dissipation; what type of secondary structures can help to attain those? 2. How much improvement in terms of multi-mode and low-frequency control will this type of secondary structure bring? 3. Will it cause high demand in secondary responses or the amount of devices? These questions are the focus of this study.

We assume that vertical irregularities in terms of inter-story stiffness and inter-module dampers within the suspended discrete modules are

acceptable, as modules protect non-structural members against excessive or even concentrated inter-story drift brought by a soft story effect, which would have caused severe damage in regular-type structures [26–28]. Moreover, the concentrated drift would not cause a P-delta effect, due to the upward delivery of vertical loads in suspension. We also assume that inter-module stiffness will not be considerably affected by non-structural members as only mechanical springs, viscous dampers and sometimes flexible pipelines exist between upper and lower modules.

On this basis, we set different levels of vertical distribution vectors for damping coefficients and inter-module stiffness as the variables in single/multiple-objective genetic-algorithm optimizations. Complex mode and time-history analyses are also carried out. The optimal vertical distributions, multi-mode control mechanism and the change on the patterns of other responses are thus revealed.

In this paper, the features of the modularized suspended building structure and the set-up of the calculation are presented in Section 2. The set-up of the single objective optimization is presented in Section 3.1; in the rest parts of Section 3, the corresponding results are presented, including the optimized performance indexes, transfer functions, and major complex modes; based on the optimized model, the effect of uncertainties of the structural parameters and the non-stationary excitations are both studied in this section. Results of multi-objective optimizations and time-history verifications are presented respectively in Section 4 and 5.

2. Modularized suspended structure, calculation model and mean square responses

Fig. 1 shows the diagram of the previously proposed modularized suspended structure. The primary structure consists of a core tube and a truss on the top, which suspends a segment of discrete prefabricated modules from a chain of steel tubes, with pin connections. Fuse-type floor cassettes connect modules to the core-tube and transfer wind loads; the fuses break and the cassettes slide during an earthquake, with mechanical springs and dampers providing inter-story stiffness and dissipation, respectively.

The protection effect of suspended modules is also illustrated in Fig. 1. A major type of mega-substructure systems develops their flexibility through the secondary structure inter-story drift that occurs entirely inside the story-space and affects non-structural members. To the contrary, the modularized solutions have an in-between low-stiffness layer to let a majority of the drift develop outside the modules, resulting in a much lower proportion of harmful drift a.

Overall, the calculation model consists of beam members, link members, lumped masses and viscous damper elements. The one-story truss with a width of 30 m is on top of the ten-story Timoshenko beam-type core-tube, reaching a total height of 44 m. The suspended segment has nine stories of rigid modules, with the bottom module connected to the core tube by horizontal links. Three layouts of dampers are set, including the D1 model with dampers connecting the bottom corner of each module to the core, the D2 model with dampers connecting each pair of upper and lower modules, and the uncontrolled (UNC) model with horizontal links substituting every single damper in the D1 model, as shown in Fig. 1.

The rotation response caused by eccentricity can be significantly reduced if the structure is properly designed. When the inter-module mechanical springs and the dampers are mostly located at the outer rim of the plan of the story, the frequency and the damping ratios of the rotary modes become much higher; given the fact that the core-tube is also stiff in terms of rotation, this effect can be neglected.

For the primary structure, when it is assumed to be linear, each story consists of a Timoshenko beam elements with a quadratic shape function and a rectangular section meshed into 1 × 6 cells (considering that the system is 2D and that the strain output is requested). The section information is listed as follows: 1.09 m × 9.2 m, $EI = 2.12 \times 10^9$ kN·m^2 and $GA = 1.25 \times 10^8$ kN. For the nonlinear type of primary structure, each story consists of an OpenSees element named nonlinearBeamColumn which is a prismatic element with the spreading of plasticity and Gauss-Lobatto quadrature integration rule, is adopted in modeling the elasto-plasticity of the primary structure. In this study, the element has 20 * 6 fibers and 5 integration points on its section.

For the secondary structure, vertical link elements are connected to upper and lower modules, providing vertical stiffness. The inter-story stiffness are provided by the linear spring elements connected between the bottom corners of the upper module and the top corners of the lower module, the sum of the stiffness of the spring elements on top of the ith story of modules denoted by k_i.

The primary structure has identical mass $m_p = 200$ t for every story; the top truss has the mass twice as a primary story; the total mass m_s of a secondary structure story is divided into 8 lumps at all corners of modules:

$$m_s = 1.22 R_m m_p \tag{1}$$

where R_m is the nominal mass ratio, and 1.22 is a coefficient considering the different numbers of primary and secondary stories. In this study, $R_m = 2$.

There are N degrees of lateral freedom and N degrees of rotational freedom for the primary structure, and there are n degrees of lateral freedom for the secondary structure (as a symmetric system subjected to asymmetric excitation, the n degrees of freedom for the left suspended segment and the other n for the right are combined to be n ones); $N = 11$ and $n = 9$ for this study. Thus, the displacement vector is

$$\mathbf{u} = \{x_{p,1}, x_{p,2}, \cdots, x_{p,N} \mid \theta_{p,1}, \theta_{p,2}, \cdots, \theta_{p,N} \mid x_{s,1}, x_{s,2}, \cdots, x_{s,n}\}^T \tag{2}$$

The dynamic equilibrium equation of the system is

$$\mathbf{M}^{\text{total}}\ddot{\mathbf{u}} + \mathbf{C}^{\text{total}}\dot{\mathbf{u}}_\mathbf{r} + \mathbf{K}^{\text{total}}\mathbf{u}_\mathbf{r} = \mathbf{F}^{\text{total}} \tag{3}$$

For ground motion excitation

$$\mathbf{M}^{\text{total}}\ddot{\mathbf{u}}_\mathbf{r} + \mathbf{C}^{\text{total}}\dot{\mathbf{u}}_\mathbf{r} + \mathbf{K}^{\text{total}}\mathbf{u}_\mathbf{r} = -\mathbf{M}^{\text{total}}\mathbf{r}\ddot{u}_g \tag{4}$$

where $\mathbf{r} = \{1, \cdots, 1 \mid 0, \cdots, 0 \mid 1, \cdots, 1\}^{\mathrm{T}}$ and $\ddot{u}_g$ is the ground acceleration.

The mass matrix is

$$\mathbf{M}^{\text{total}} = \left(\begin{array}{ccc|c|ccc} m_{p,1} & \mathrm{L} & 0 & & & & \\ \mathrm{M} & \mathrm{O} & \mathrm{M} & 0 & & 0 & \\ 0 & \mathrm{L} & m_{p,N} & & & & \\ \hline & 0 & & \mathbf{J_p}' & & 0 & \\ \hline & & & & m_{s,1} & \mathrm{L} & 0 \\ & 0 & & 0 & \mathrm{M} & \mathrm{O} & \mathrm{M} \\ & & & & 0 & \mathrm{L} & m_{s,n} \end{array}\right) \tag{5}$$

$$\mathbf{J}_\mathbf{p}' = \mathbf{J_p} + \mathbf{J_{ps}} \tag{6}$$

$$\mathbf{J_p} = \mathrm{diag}[J_1, J_2, \cdots, J_N] \tag{7}$$

$$\mathbf{J_{ps}} = \mathrm{diag}\left[0, 0, \cdots, nm_s\left(\left(\frac{b_2}{2}\right)^2 + \left(\frac{b_2}{2} + b_1\right)^2\right)\right] \tag{8}$$

where $\mathbf{J}_\mathbf{p}'$ is the moment of inertia matrix, $\mathbf{J_{ps}}$ is the contribution by secondary structure and J_i ($i = 1, 2, \cdots, N$) is the moment of inertia of ith primary mass (in this study $J_i = 0$ ($i = 1, 2, \cdots, N$), but non-zero values may be applied when, in other cases, some modules are cantilevered to the core, adding up to non-negligible rotary inertia).

First, the stiffness matrix without the contribution of dampers and horizontal links is

$$\mathbf{K}_0^{\text{total}} = \begin{bmatrix} \mathbf{K_p} & \mathbf{0} \\ \mathbf{0} & \mathbf{K_s} \end{bmatrix} + \left[\begin{array}{ccc} \mathbf{A_0} & \mathbf{A_2} & \mathbf{A_3} \\ \mathbf{A_2}^{\mathrm{T}} & \mathbf{A_1} & \mathbf{A_4} \\ \hline \mathbf{A_3}^{\mathrm{T}} & \mathbf{A_4}^{\mathrm{T}} & \mathbf{0} \end{array}\right] \tag{9}$$

Table 1
Optimization problems.

Single-objective	Dual-objective	Quintuple-objective
minimize MMSDP $_{R_c,R_k,\mathbf{r}_c,\mathbf{r}_k}$	minimize {MMSDP, MMSDS} or minimize {MMSDP, $\sum_i c_i$} $_{R_c,R_k,\mathbf{r}_c,\mathbf{r}_k}$	minimize {MMSDP,MMSDS, $\sum_i c_i$, MMSAS,MMSUR} $_{R_c,R_k,\mathbf{r}_c,\mathbf{r}_k}$
subjected to:	$R_c \in [0, 100 + 300R_m]$	
	$R_k \in [10R_m, 400 + 400R_m]$	
	$r_{c,i} \in A_c$ ($i = 1\cdots n$)*	
	$r_{k,i} \in A_k$ ($i = 1\cdots n$)**	

* A_c = the set of allowable values for $r_{c,i}$.
** A_k = the set of allowable values for $r_{k,i}$.

Table 2
Allowable range of elements in distribution vectors.

Vertical distribution level		A_k for $r_{k,i}$	A_c for $r_{c,i}$	Number of initial samples
NVD	(non-vertically distributed)	Constant*	Constant**	20
VD-AMP low	(low allowable amplitude)	[1, 3]	[1, 5]	50
VD-AMP high	(higher allowable amplitude)	[1, 15]	[1, 18]	60
VD-Bind	(direct binding)	{1, + ∞}	Constant**	30
VD-LEV	(scattered levels of allowable values)	{1, 50, 100}	{1, 225, 450}	50
VD	(full vertical distribution)	[1, 100]	[1, 450]	100

* Constant vector $\mathbf{r}_k = \{3, 3, 2, 1, 1, 2, 3, 3\}^T$.
** For D1 model, constant vector $\mathbf{r}_c = \{1, 1, 1, 1, 1, 1, 1, 0\}^T$; for D2 model, constant vector $\mathbf{r}_c = \{0, 1, 1, 1, 1, 1, 1, 0\}^T$, as adopted in the previous study [14].

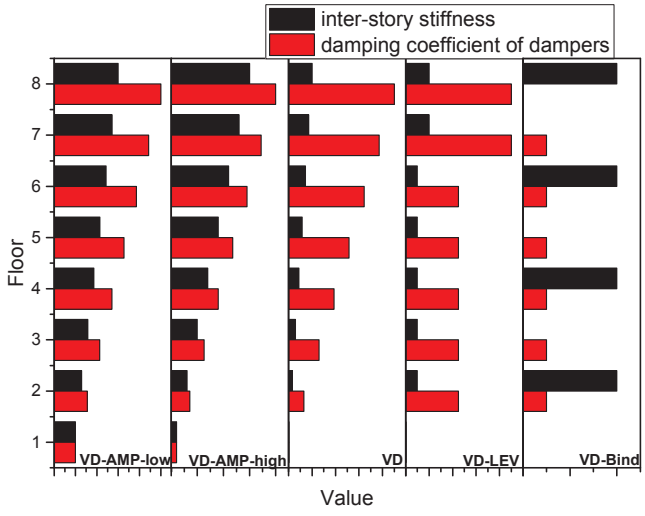

Fig. 2. Illustrative vertical distributions of different distribution levels.

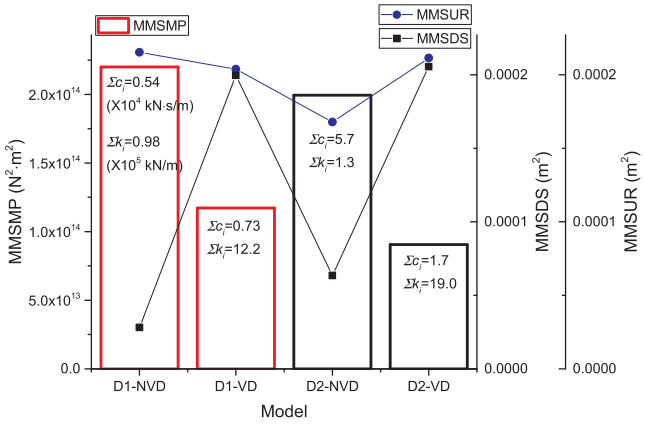

Fig. 3. Responses in single-objective optimization (aspect-1: layout of dampers) ($R_m = 2$).

where $\mathbf{A}_j (j = 0, 1, \cdots, 4)$ arises from the interaction between primary and secondary structures, $\mathbf{K_p}$ is the $2N \times 2N$ stiffness matrix of primary structure, and $\mathbf{K_s}$ is the $n \times n$ stiffness matrix of secondary structure when fixed to the transfer truss.

The matrixes $\mathbf{K_s}$ and $\mathbf{A}_j (j = 0, 1, \cdots, 4)$ are expressed as follows:

$$\mathbf{K_s} = \begin{bmatrix} k_1 & -k_1 & \cdots & \cdots & 0 \\ -k_1 & k_1+k_2 & -k_2 & & \vdots \\ \vdots & -k_2 & \ddots & \ddots & \vdots \\ \vdots & & \ddots & \ddots & -k_{n-1} \\ 0 & \cdots & \cdots & -k_{n-1} & k_{n-1}+k_n \end{bmatrix} \tag{10}$$

$$a_{0,NN} = k_n \tag{11}$$

$$a_{2,NN} = k_n \cdot (h_n - H) \tag{12}$$

$$a_{3,Nn} = -k_n \tag{13}$$

$$a_{4,Ni} = \begin{cases} k_i(h_{i+1} - h_i) + k_{i-1}(h_{i-1} - h_i) & (1 < i < n) \\ k_1(h_2 - h_1) & (i = 1) \\ k_n(H - h_n) + k_{n-1}(h_{n-1} - h_n) & (i = n) \end{cases} \tag{14}$$

$$a_{1,NN} = \sum_{i=1}^{n} a_{4,Ni} \cdot (H - h_i) \tag{15}$$

where $i = 1, 2, \cdots, n$, with all other elements being 0.

With $\mathbf{M^{total}}$ and $\mathbf{K^{total}}$ derived, the damping matrix without the contribution of dampers can be constructed in the Rayleigh form.

$$\mathbf{C_0^{total}} = a\mathbf{M^{total}} + b\mathbf{K^{total}} \tag{16}$$

We now discuss the complete system with additional dampers. For elasto-viscous dampers,

$$f_{d,ij} = k_{d,ij} \cdot x_{r,ij} + c_{d,ij} \cdot \dot{x}_{r,ij}^{\alpha} \tag{17}$$

where f_{di} is the axial force of the damper connecting the ith primary story and the jth secondary story, $x_{r,ij}$ is the relative horizontal displacement between damper ends and α is the damping exponent.

Then the contribution of dampers to the stiffness matrix and the damping stiffness matrix is derived, as shown in the second terms of the following equations.

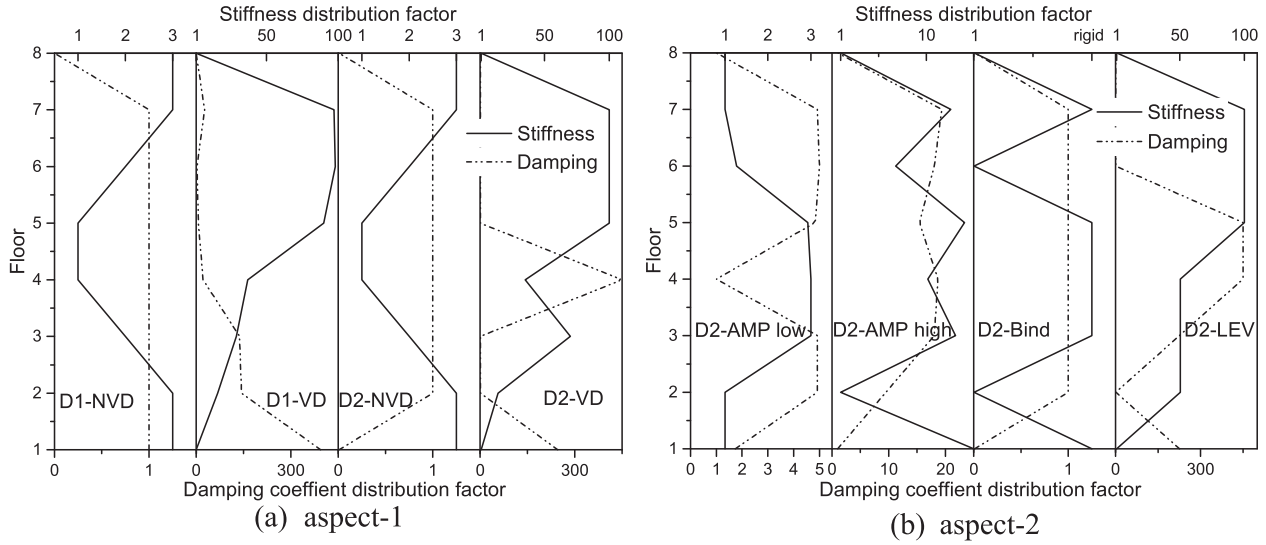

Fig. 4. Optimal vertical distribution vectors (aspect-1: layout of dampers and aspect-2: level of vertical distribution) ($R_m = 2$).

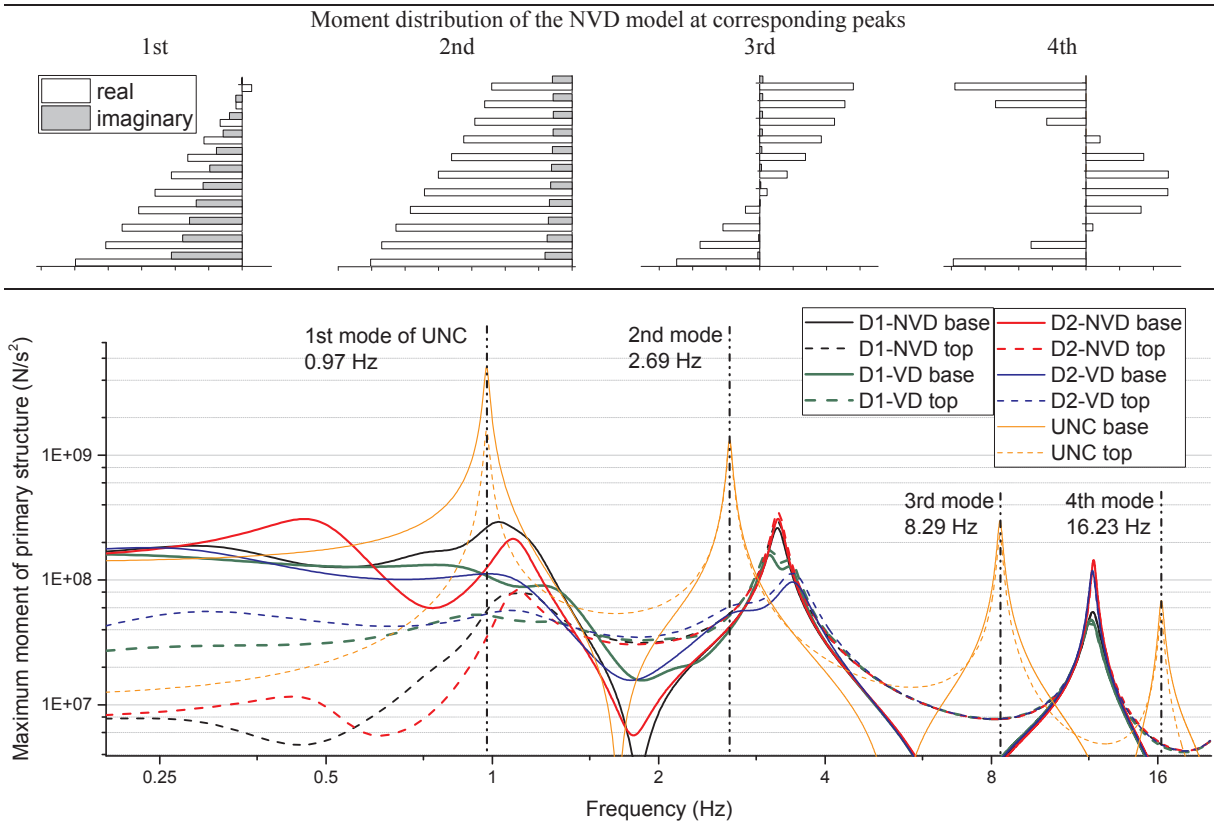

Fig. 5. Amplitudes of optimized transfer functions of the primary structure moment ($R_m = 2$).

$$\mathbf{K}^{\text{total}} = \mathbf{K}_0^{\text{total}} + \left[\begin{array}{cc|c} \mathbf{A}_{\mathbf{d0}} & \mathbf{A}_{\mathbf{d2}} & \mathbf{A}_{\mathbf{d3}} \\ \mathbf{A}_{\mathbf{d2}}{}^{\mathrm{T}} & \mathbf{A}_{\mathbf{d1}} & \mathbf{A}_{\mathbf{d4}} \\ \hline \mathbf{A}_{\mathbf{d3}}{}^{\mathrm{T}} & \mathbf{A}_{\mathbf{d4}}{}^{\mathrm{T}} & \mathbf{A}_{\mathbf{d5}} \end{array}\right] \tag{18}$$

$$\mathbf{C}^{\text{total}} = \mathbf{C}_0^{\text{total}} + \left[\begin{array}{cc|c} \mathbf{B}_{\mathbf{d0}} & \mathbf{B}_{\mathbf{d2}} & \mathbf{B}_{\mathbf{d3}} \\ \mathbf{B}_{\mathbf{d2}}{}^{\mathrm{T}} & \mathbf{B}_{\mathbf{d1}} & \mathbf{B}_{\mathbf{d4}} \\ \hline \mathbf{B}_{\mathbf{d3}}{}^{\mathrm{T}} & \mathbf{B}_{\mathbf{d4}}{}^{\mathrm{T}} & \mathbf{B}_{\mathbf{d5}} \end{array}\right] \tag{19}$$

For D1 model, one damper at each floor connects primary and secondary structure. The damper at ith floor is denoted as ith damper.

$$a_{d0,ii} = k_{d,ij} \tag{20}$$

$$a_{d3,ij} = -k_{d,ij} \tag{21}$$

$$a_{d5,jj} = k_{d,ij} \tag{22}$$

where $i = 1, 2, \cdots, n$ with all other elements being 0.

For D2 model, each damper connects a pair of adjacently upper and lower modules. The damper connecting the modules at the ith and $(i+1)$th floors is denoted as the ith damper.

$\mathbf{A_{d5}}$ is in the same form as $\mathbf{K_s}$ in Eq. (10), with k_i substituted by $k_{d,ij}$. Elements in $\mathbf{A_{d0}}$ to $\mathbf{A_{d4}}$ are in the same form as shown in Eqs. (10)–(15) respectively, with k_i substituted by $k_{d,ij}$. Herein $i = 1, 2, \cdots, n$ with all

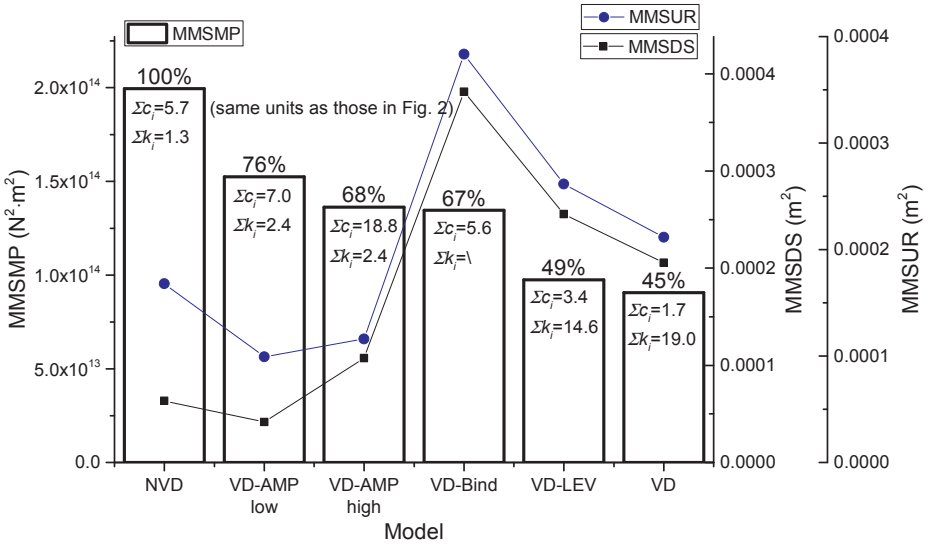

Fig. 6. Responses in single-objective optimization of the D2 models (aspect-2: level of vertical distribution) ($R_m = 2$).

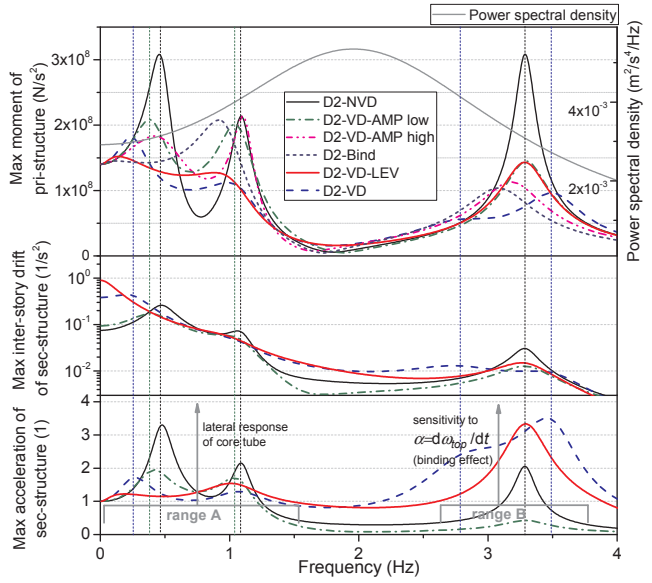

Fig. 7. Amplitudes of optimized transfer functions of different response quantities and the power spectral density function (aspect-2: level of vertical distribution) ($R_m = 2$).

other elements being 0.

Herein $\mathbf{B}_{\mathbf{d}j}$ and the aforementioned $\mathbf{A}_{\mathbf{d}j}$ ($j = 0, 1, \cdots, 5$) have parallel meanings and the same form, with each $k_{d,i}$ being substituted by $c_{d,i}$.

With derivation almost complete except for the bottom links, the condensation is carried out by setting connected degrees of freedom equal. These degrees of freedom are the 1st and the $(2N + 1)$th in this case.

$$u_{r,2N+1} = u_{r,1} \tag{23}$$

The $(2N + 1)$th degree of freedom $u_{r,2N+1}$ is deleted. Relevant elements in matrixes are modified as follows.

$$\overline{m}_{i1}^{total} = m_{i1}^{total} + m_{i(2N+1)}^{total} \quad (i = 1, \cdots, 2N + n) \tag{24}$$

$$\widehat{m}_{1i}^{total} = \overline{m}_{1i}^{total} + \overline{m}_{(2N+1)i}^{total} \quad (i = 1, \cdots, 2N,\ 2N + 2, \cdots, 2N + n) \tag{25}$$

Thus the $(2N + n - 1) \times (2N + n - 1)$ matrix $\widehat{\mathbf{M}}^{\mathbf{total}}$ is derived. $\widehat{\mathbf{C}}^{\mathbf{total}}$ and $\widehat{\mathbf{K}}^{\mathbf{total}}$ are also derived in similar manner. For load excitation,

$$\widehat{f}_1^{total} = f_1^{total} + f_{2N+1}^{total} \tag{26}$$

For ground motion excitation,

$$\widehat{r}_1 = r_1 + r_{2N+1} \tag{27}$$

For multiply connected systems (e.g., the UNC), the above steps are repeated for each connection. Thus, the complete equation of dynamic equilibrium (28) is derived:

$$\widehat{\mathbf{M}}^{\mathbf{total}}\ddot{\mathbf{u}}_{\mathbf{r}} + \widehat{\mathbf{C}}^{\mathbf{total}}\dot{\mathbf{u}}_{\mathbf{r}} + \widehat{\mathbf{K}}^{\mathbf{total}}\mathbf{u}_{\mathbf{r}} = -\widehat{\mathbf{M}}^{\mathbf{total}}\hat{\mathbf{r}}\ddot{u}_g \tag{28}$$

which is subsequently referred to as:

$$\mathbf{M}\ddot{\mathbf{u}}_{\mathrm{r}} + \mathbf{C}\dot{\mathbf{u}}_{\mathrm{r}} + \mathbf{K}\mathbf{u}_{\mathrm{r}} = -\mathbf{M}\mathbf{r}\ddot{u}_g \tag{29}$$

The damping matrix consists of the Rayleigh-form contribution and the supplemental dampers' contribution $\mathbf{C}_{\mathrm{d}}$, wherein the dampers are linear viscous.

$$\mathbf{C} = \alpha\mathbf{M} + \beta\mathbf{K} + \mathbf{C}_{\mathrm{d}} \tag{30}$$

Via Fourier transform $\mathbf{u}_{\mathrm{r}} \Rightarrow \mathbf{H}_{\mathrm{ur}}(\boldsymbol{\omega})$ and $u_g \Rightarrow H_{ug}(\omega)$, the frequency response is derived.

$$\mathbf{H}_{\mathrm{ur}}(\boldsymbol{\omega}) = (-\omega^2\mathbf{M} + i\omega\mathbf{C} + \mathbf{K})^{-1} \cdot \omega^2\mathbf{M}\mathbf{r}H_{ug}(\omega) \tag{31}$$

Other responses can be derived by the linear combinations of $\mathbf{H}_{\mathrm{ur}}(\boldsymbol{\omega})$ and $\mathbf{r}H_{ug}(\omega)$.

Thus, the frequency response function (i.e. the transfer function) and the corresponding mean square value are defined as follows:

$$\widehat{\mathbf{H}}_{\mathrm{ur}}(\boldsymbol{\omega}) = \frac{\mathbf{H}_{\mathrm{ur}}(\boldsymbol{\omega})}{-\omega^2 H_{ug}(\omega)} \tag{32}$$

$$\sigma_i^2 = \int_{-\infty}^{\infty} \widehat{h}_i(\omega)^* \cdot \widehat{h}_i(\omega) S_g(\omega)\mathrm{d}\omega \tag{33}$$

where $S_g(\omega)$ is the power spectral density function of ground motion and $\widehat{\mathbf{H}}(\boldsymbol{\omega})^*$ is the conjugate of $\widehat{\mathbf{H}}(\boldsymbol{\omega})$. In this study, The Kanai-Tajimi type power spectral density (PSD) function is adopted:

$$S_g(\omega) = S_0 \cdot \left(1 + 4\xi_g^2\left(\frac{\omega}{\omega_g}\right)^2\right) \Bigg/ \left(\left(1 - \left(\frac{\omega}{\omega_g}\right)^2\right)^2 + 4\xi_g^2\left(\frac{\omega}{\omega_g}\right)^2\right) \tag{34}$$

where $\omega_g = 15$ rad/s, $\xi_g = 0.6$ and $S_0 = 2.92 \times 10^{-3}$ m²/s⁴/Hz.

The objectives of optimization include: (1) the maximum mean square value of the moment of the primary structure (MMSMP, defined by Eq. (35)); (2) the maximum mean square value of the inter-story drift of the secondary structure (MMSDS, defined by Eq. (36)); (3) the

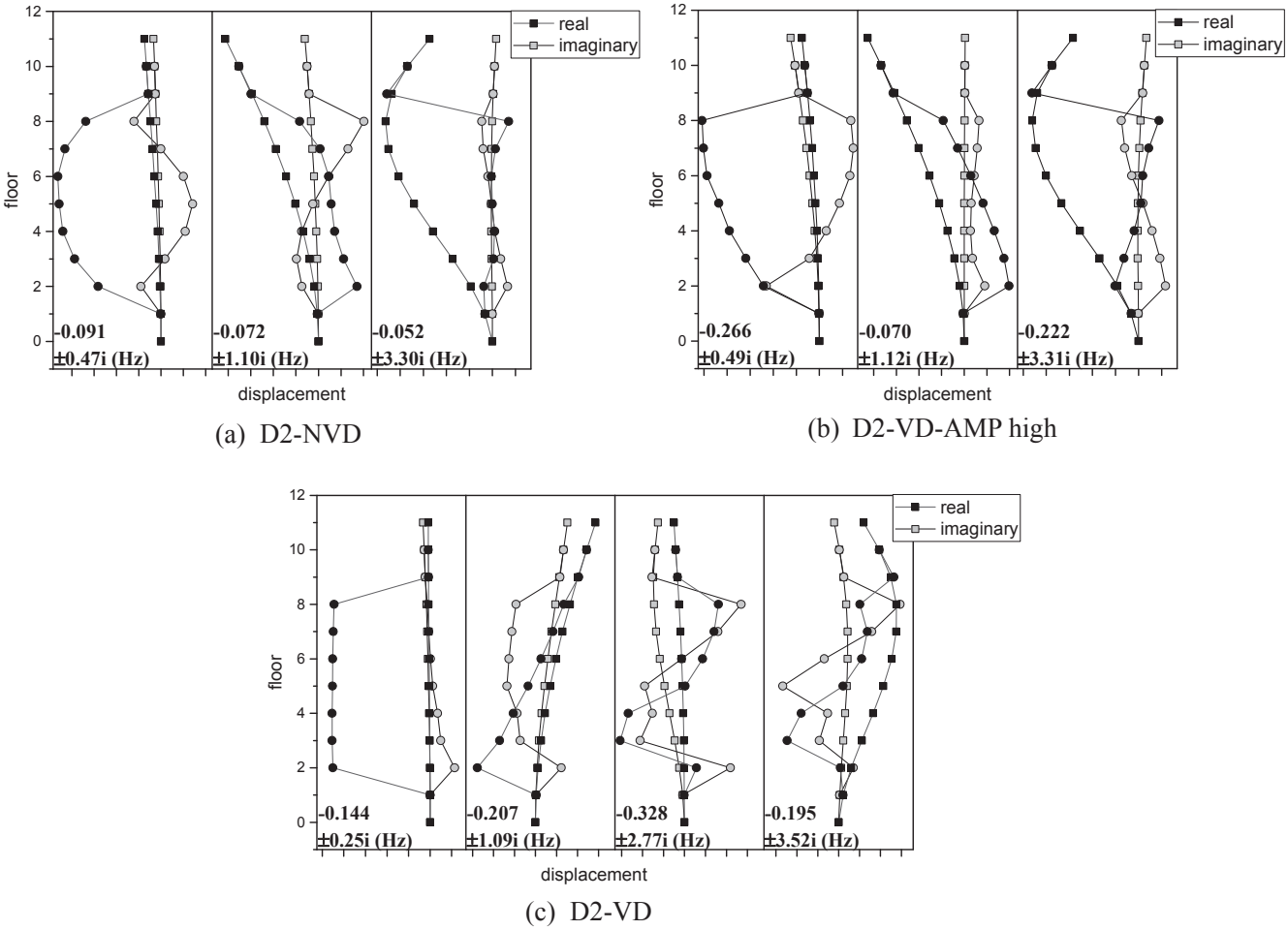

Fig. 8. Major complex modes of optimized models.

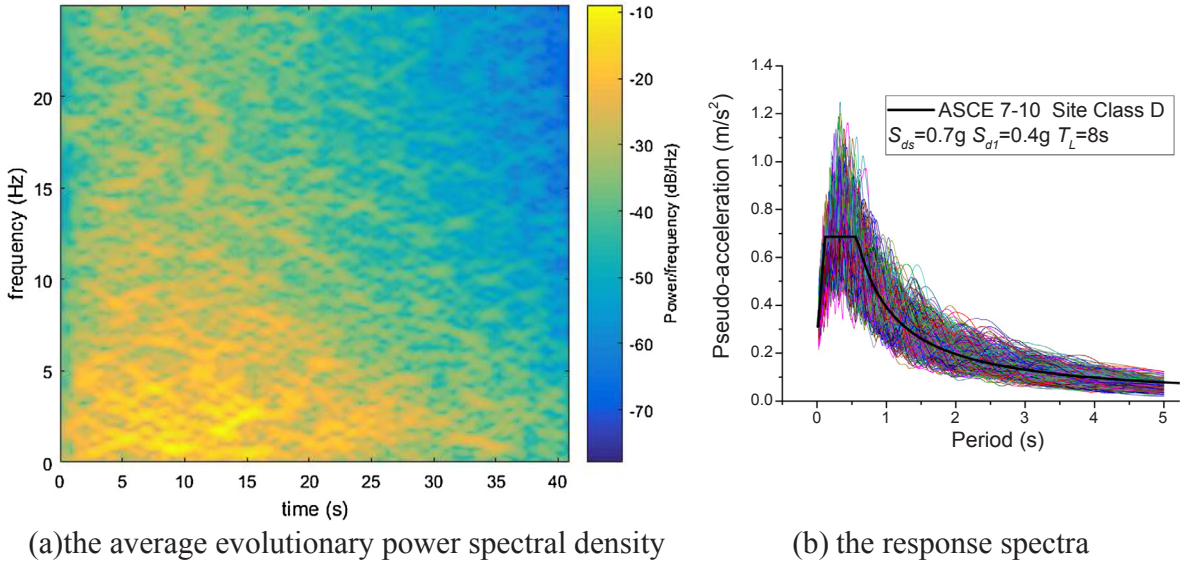

Fig. 9. The average evolutionary power spectral density and the response spectra of the 400 randomly generated artificial ground motions.

maximum mean square value of the absolute acceleration of the secondary structure (MMSAS, defined by Eq. (37)); and (4) the maximum mean square value of the relative displacement between primary and the secondary structure (MMSUR, defined by Eq. (38)).

$$\text{MMSMP} = \max_i \sigma^2_{\text{mp},i} = \max_i \int_{-\infty}^{\infty} \hat{h}_{\text{mp},i}(\omega)^* \cdot \hat{h}_{\text{mp},i}(\omega) S_g(\omega) \mathrm{d}\omega \tag{35}$$

where $\hat{h}_{\text{mp},i}(\omega)$ is the transfer function of the moment of the ith story in the primary structure, as in (32).

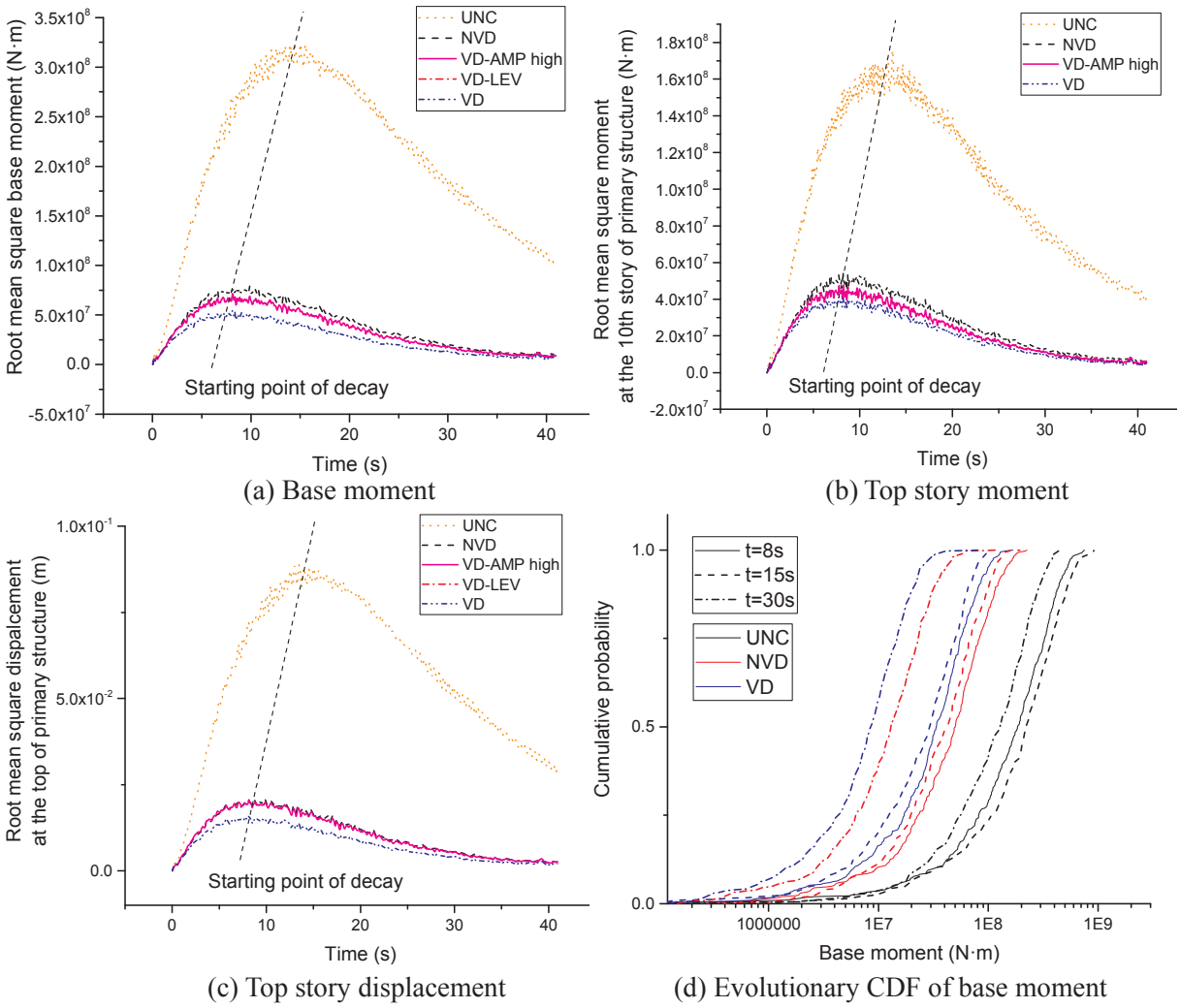

Fig. 10. The root mean square curves of the time-history responses under the excitation of the 400 randomly generated artificial ground motions and the evolutionary cumulative probability curves.

Table 3
The probability distributions of random variables.

Variable	Inter-module stiffness scalar R_k	Damping coefficient scalar R_c	Nominal mass ratio R_m	*EI* of the primary structure
Probability distribution	Log-normal	Normal	Normal	Normal
Coefficient of variation	0.08	0.3	0.1	0.2

$$\mathrm{MMSDS} = \max_i \sigma^2_{\mathrm{ds},i} = \max_i \int_{-\infty}^{\infty} \hat{h}_{\mathrm{ds},i}(\omega)^* \cdot \hat{h}_{\mathrm{ds},i}(\omega) S_g(\omega) \mathrm{d}\omega \tag{36}$$

$$\mathrm{MMSAS} = \max_i \sigma^2_{\mathrm{as},i} = \max_i \int_{-\infty}^{\infty} \hat{h}_{\mathrm{as},i}(\omega)^* \cdot \hat{h}_{\mathrm{as},i}(\omega) S_g(\omega) \mathrm{d}\omega \tag{37}$$

$$\mathrm{MMSUR} = \max_i \sigma^2_{\mathrm{ur},i} = \max_i \int_{-\infty}^{\infty} \hat{h}_{\mathrm{ur},i}(\omega)^* \cdot \hat{h}_{\mathrm{ur},i}(\omega) S_g(\omega) \mathrm{d}\omega \tag{38}$$

3. Single-objective optimization analysis

3.1. Set-up of the optimization

The MOGA-II genetic optimization algorithm [29], which consists of four major operators: classical crossover, directional crossover, mutation and selection, is adopted in this study. The genetic mutation of MOGA-II procedure consists of classical mutation and directional mutation wherein a better direction to mutate genes is determined by judging a pair of parental samples. Though more advanced and efficient algorithms exist for various optimization scenarios, the MOGA-II algorithm has been proved to be more efficient than those with mere classical mutation, and it also provides satisfactory global convergence when the convexity of the objective function is highly complicated.

The mean-square structural responses [30,31] were the objective functions to be minimized, since genetic algorithms [32–34] and such objective functions have shown satisfactory effectiveness in capturing the potential of structural control. Ranges for variables were based on practical considerations, and Latin hypercube sampling was adopted to generate a suitable amount of random samples. The amount of samples is listed in Table 2. After convergence, another smaller set of initial samples were generated and another round of optimization was carried out to check whether the optimums of the two rounds coincide; the negative answer would indicate local convergence.

Two scalars and two distribution vectors of the secondary structure parameters, namely, R_k, R_c, $\mathbf{r}_k$ and $\mathbf{r}_c$, are set as optimizing variables; R_k and R_c are stiffness and damping scalars; $\mathbf{r}_k$ and $\mathbf{r}_c$ are the corresponding

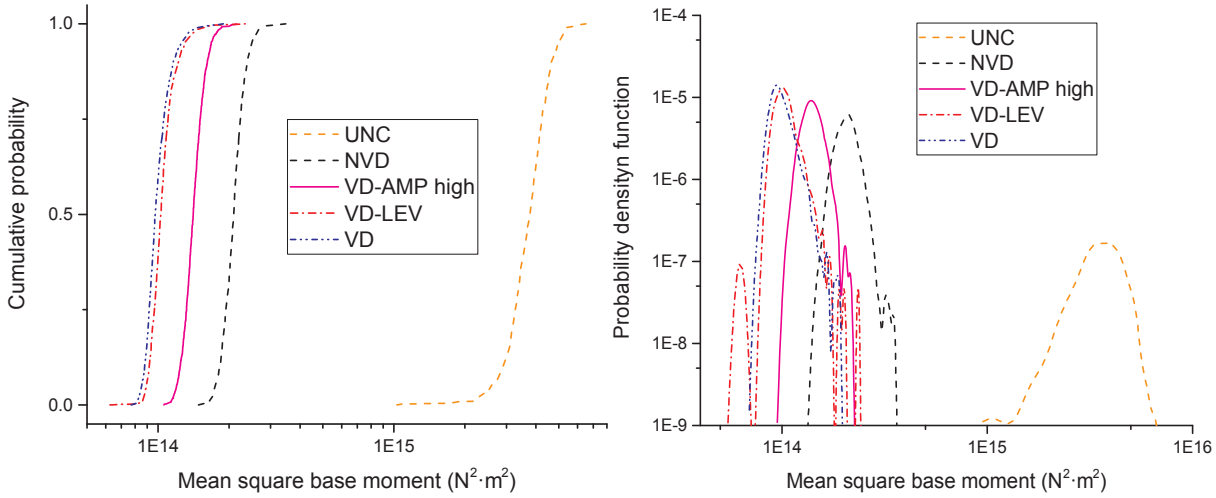

(a) Cumulative probability curves (b) Probability density function curves

Fig. 11. The cumulative probability curves and probability density function curves of the MMSDP.

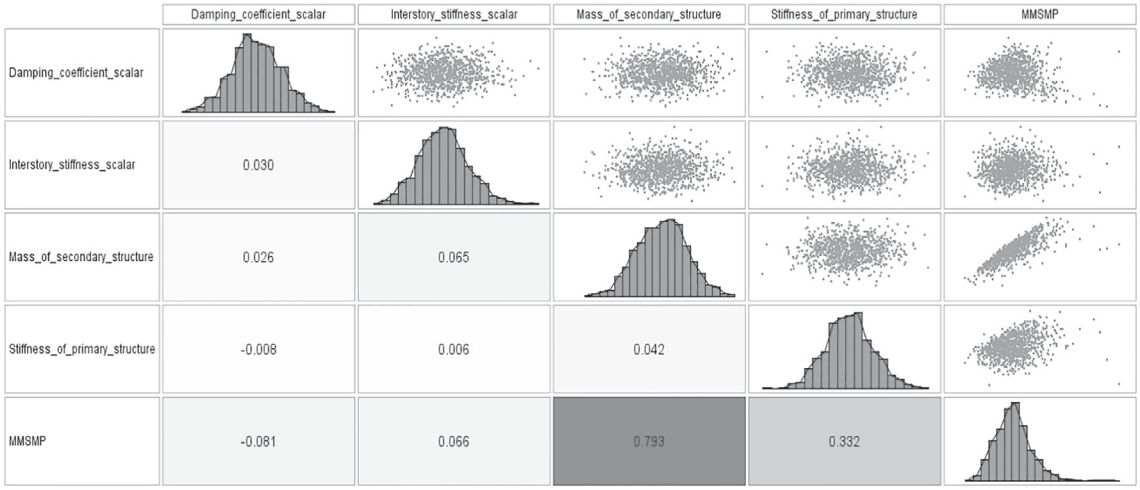

(a) The UVD model

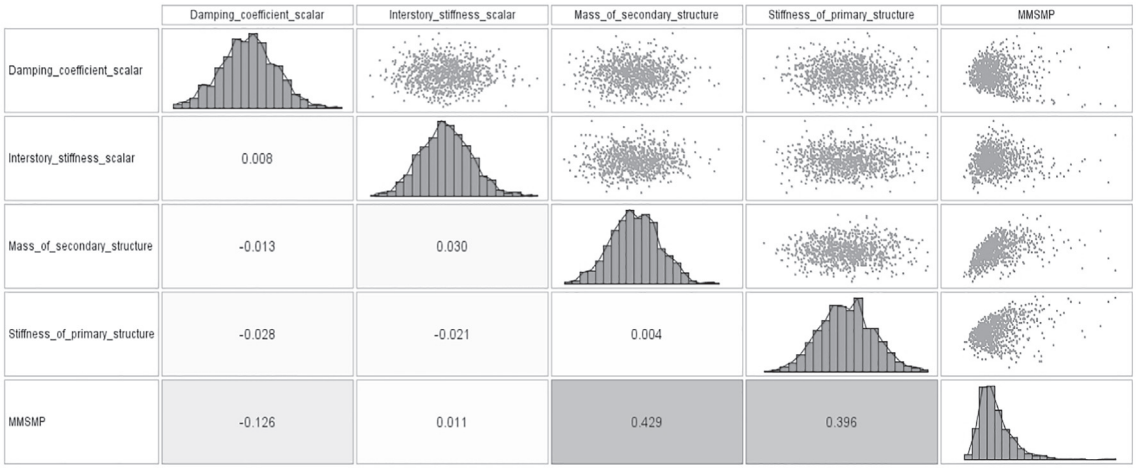

(b) The VD model

Fig. 12. The scatter matrix charts with probability density histograms, scatter plots and the Pearson Correlation values.

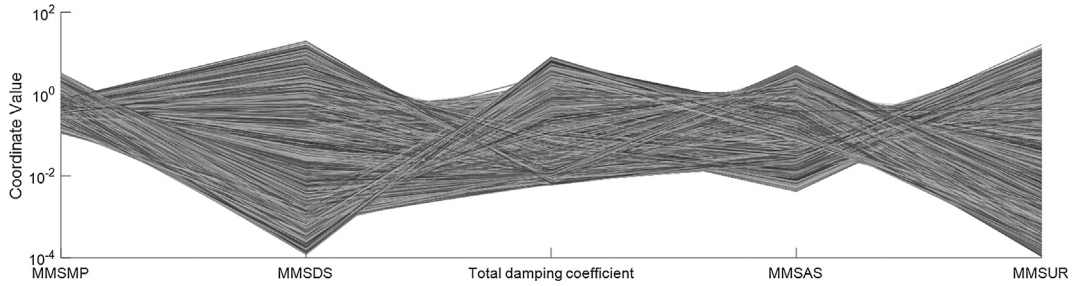

Fig. 13. Parallel coordinate plot of the quintuple-objective Pareto set of the D2-VD-AMP low model (11760 Pareto solutions).

Table 4
The trade-off indexes of the D2-VD-AMP low model among the five objectives.

	Objective 1: MMSMP	Objective 2: MMSDS	Objective 3: $\sum_i c_i$	Objective 4: MMSAS	Objective 5: MMSUR
Objective 1	–	0.526	0.664	**0.241**	0.523
Objective 2	0.526	–	0.671	0.641	**0.033**
Objective 3	0.664	0.671	–	0.620	0.677
Objective 4	**0.241**	0.641	0.620	–	0.636
Objective 5	0.523	**0.033**	0.677	0.636	–

The bold denotes low trade-off index.

vertical distribution vectors.

Inter-story stiffness k_i and viscous damping coefficients of dampers c_i in the ith story are determined respectively as:

$$k_i = R_k \times r_{k,i} \times 10^2 \text{ kN/m} \tag{39}$$

$$c_i = R_c \times r_{c,i} \times 10 \text{ kN·s/m} \tag{40}$$

Single/dual/quintuple-objective optimizations are all discussed in Section 3 and 4, and the definitions of the optimization problems are listed in Table 1.

We set six different levels of the vertical distribution vectors, as shown in Table 2, to account for the effect of different degrees of vertical irregularities, because the continuous and infinitely wide range of values does not seem possible considering the constraint on numbers and available specifications of springs and dampers. The illustrative examples of vertical distributions are depicted in Fig. 2, for each distribution level, for a more intuitive comprehension.

Models are differentiated in these 2 aspects: the layout of dampers and the level of distribution. For instance, a model named D1-NVD has the first type of damper layout and optimized parameters without considering vertical distribution.

3.2. Result of single-objective optimization

3.2.1. Overall result and aspect-1: layout of dampers

Three major responses of the optimized models, along with the sums of the stiffness and damping coefficients, are shown in Fig. 3. Considerable improvement in the primary structure performance can be achieved by optimizing vertical distribution, at the expense of much higher inter-story drift within the secondary structure, but the demands of relative displacement between the primary and secondary structures are almost unchanged, indicating concentrations of drift. Such effects are roughly the same for both layouts of dampers, while the D2 layout outperforms the D1 slightly. More springs are demanded in the VD models, while the demand for dampers changes in quite different patterns for different layouts and it is much reduced by vertical distribution in the D2 layout.

For those models, optimal vertical distributions of the secondary structure stiffness and viscous damping coefficients are shown in Fig. 4(a). The VD models experience drastic changes in the elements at lower stories while the upper parts stay almost constant. The upper stories have higher stiffness (except for the top) and very low damping coefficients, while high damping appears in lower stories. Roughly, the peaks of one parameter tend to coincide with the other's troughs, which makes the pre-set distributions of the NVD models reasonable, as they more or less obey this trend [14]. Actually, a similar trend exists in the optimization of shear-type buildings [35,36], where the layout of dampers is similar to D2 but in the primary structure, with the objective being the minimization of the maximum inter-story drift. Therefore, it can be expected that such a pattern is also effective in preventing excessively increased secondary drift in the D2 model in spite of the increase shown in Fig. 3. It is confirmed in Section 4.2 of multi-objective optimizations.

Amplitudes of the optimized transfer functions are shown in Fig. 5, with both the base and the top moment of the primary structure plotted. The NVD models outperform the UNC model at around the first several peaks, showing a multi-mode control effect, while the VD models represent a further improvement, except at peaks around 12 Hz. For the controlled models, low-frequency responses are not dominant, and the moment of the top story grows in the higher frequency range. It is comparatively trivial around 1 Hz, but it slightly exceeds the base moment in the next peak before the two become roughly the same in the even next. This is mainly due to the increasing rotary acceleration of the transfer truss on the top, which causes the vertical inertia of the suspended segment; it leads to a greater demand for hanging members and transfer truss strengths. However, such an unpleasant effect is designedly emphasized by the wider-than-usual model in this study.

3.2.2. Aspect-2: level of vertical distribution

For brevity, we focus henceforth on only the D2 models. Levels of vertical distributions show a strong influence on the optimization results, as shown in Fig. 6. As the degree of allowable vertical irregularity increases, the moment in the primary structure decreases, while the other two response quantities exhibit a different trend, as they are more dependent on the distribution strategies. A lower allowable amplitude of distribution vectors leads to smaller secondary responses, while fewer allowable levels of values result in an opposite effect. Compared with the LEV and VD models, the AMP models require much lower inter-module stiffness but many more dampers.

At the intermediate levels, the aforementioned trends of distribution vectors are weakened, as shown in Fig. 4(b). The LEV model exhibits distributions similar to those of the VD model, while the AMP low model better obeys the aforementioned "peak to trough" trend. Thus, the LEV model has a lower primary response, and the AMP low model has lower secondary responses. Although the LEV and VD models show a similar "bound block" in higher stories, the Bind model shows a different pattern of binding due to its pre-set distribution of dampers, indicating the strong interaction between stiffness and dampers.

As can be observed in the low-frequency sections of the transfer functions' amplitudes shown in Fig. 7, other models tend to have lower peaks instead of deeper troughs of the primary structure moments, when compared with the NVD model. They show similar trends with different amplitudes. However, only the Bind model fails to form its first trough around 0.7 Hz due to its rigidity and only the VD model

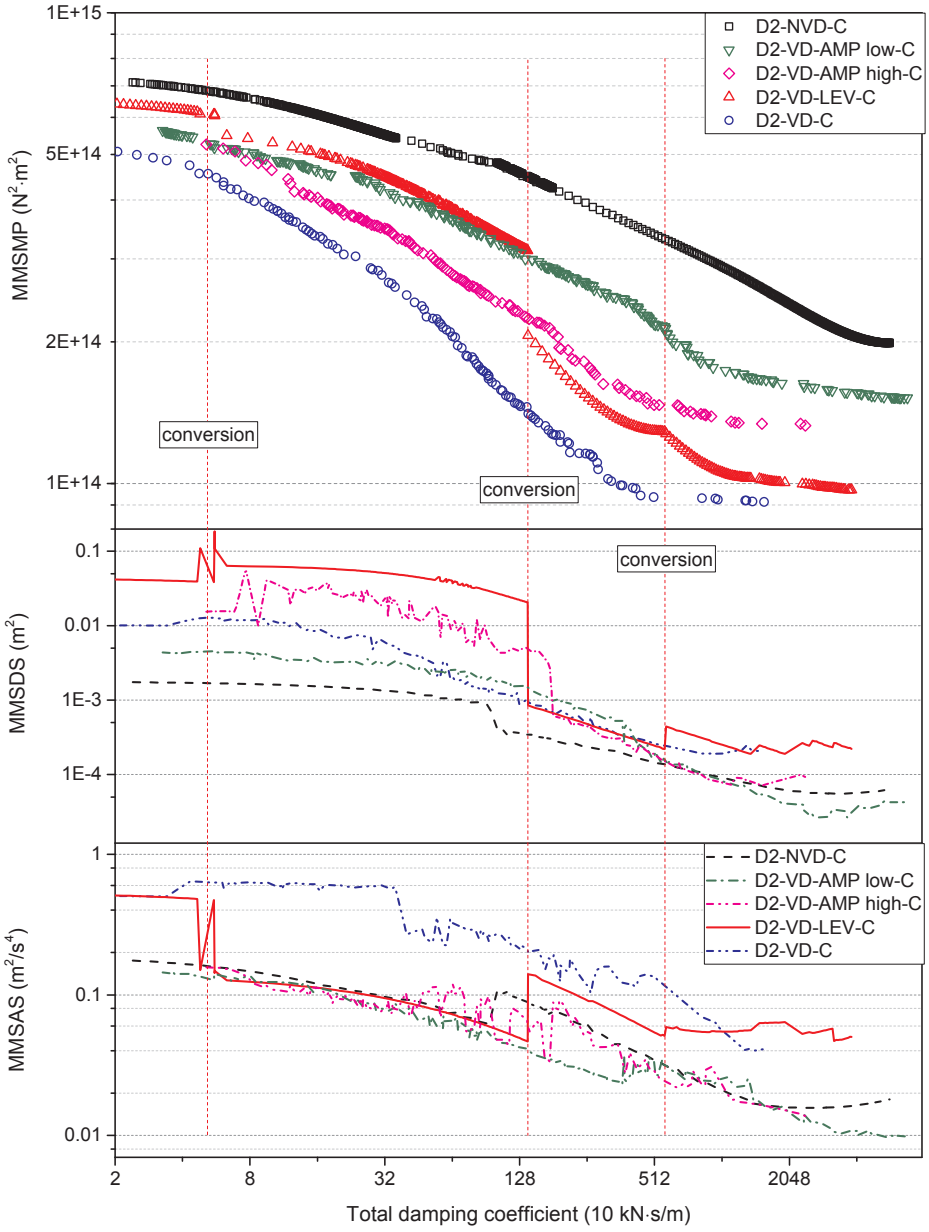

Fig. 14. MMSMP-$\sum_i c_i$ Pareto fronts with corresponding MMSDS and MMSAS responses ($R_m = 2$).

manages to form two minor peaks around 3.2 Hz showing the best multi-mode control effect. As for secondary inter-story drifts and accelerations, peaks emerge at mostly the same frequencies as those of the primary moment. That results from the fact that each peak is dominated by one major mode, which has considerable responses in both parts of the structure. Compared with the NVD model, the VD and LEV models experience larger secondary drifts in the low-frequency range and larger secondary accelerations at higher frequencies, while the AMP low model has appealing secondary responses in the entire range. Acceleration performances of models rank quite differently in different frequency ranges ("range A" and "range B" as shown in Fig. 7), because module accelerations are mainly affected by the lateral response of the core tube in "range A" while models with strong binding effects are more susceptible to the rotary accelerations of the top truss in "range B".

3.2.3. Major complex modes

Fig. 8 shows the optimized complex modes that contribute to low-frequency peaks and the corresponding eigenvalues, with $R_m = 2$. Thus, four modes are included for the VD model and three for the NVD and AMP high models respectively. All modes, except the 3.3 Hz mode of the NVD model, show considerable responses of the secondary structure. For the other two models, both the primary and the secondary structure responses turn gradually into their respective higher modes as frequency increases, but the secondary structure of the NVD model experiences a swift change into very high modes and the mode spacing is condensed between the first two peaks of transfer function curve. To the contrary, with the optimal vertical distributions of parameters, modes of the secondary structures are well distributed in frequency domain. As a result, the higher modes are well-tuned and strong at dissipation, as indicated by the gradually increasing amplitude of the imaginary component, leading to better multi-mode control effects.

3.3. Performance of the optimized models under non-stationary excitations

The aforementioned optimization is carried out using the stationary power spectral density function, to attain high calculation efficiency in frequency domain. However, strong ground motions are evolutionary

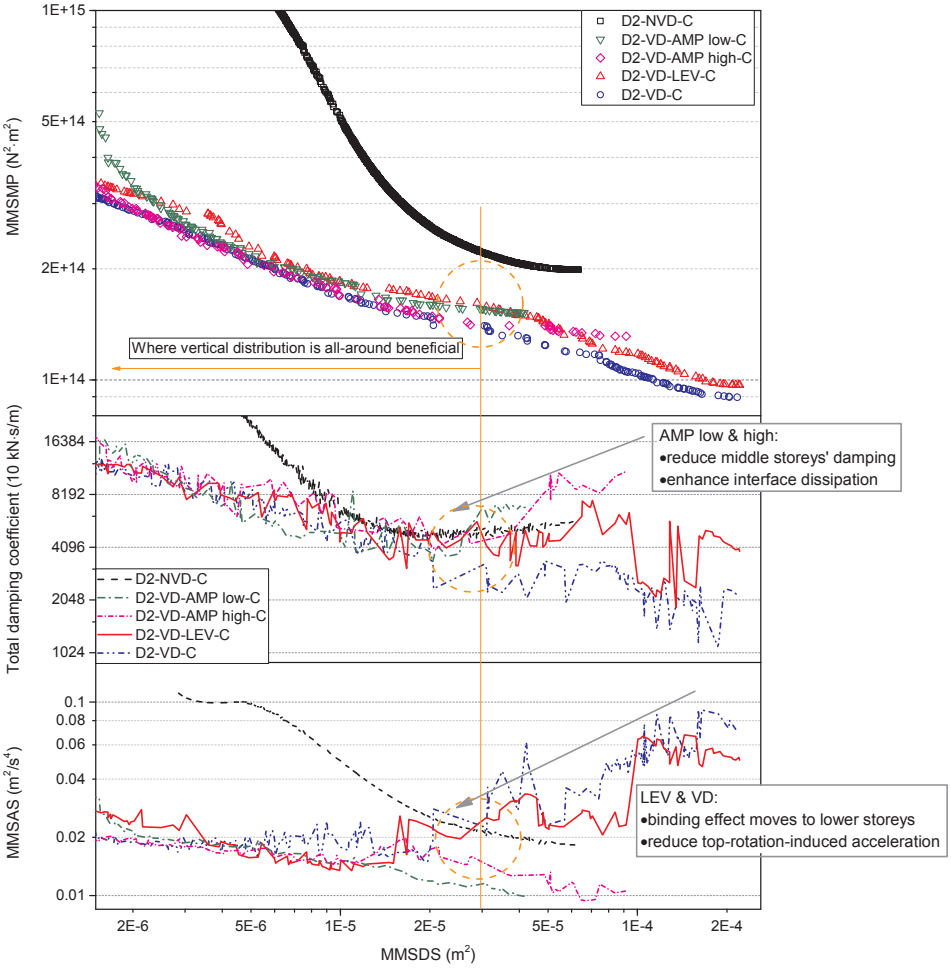

Fig. 15. MMSMP-MMSDS Pareto fronts with corresponding total damping coefficients and MMSAS responses ($R_m = 2$).

along time and the evolutionary trends depend on frequency contents, and thus the stationary analysis has yet to capture the full seismic features. This subsection aims at verifying the performance of the optimized models when they are subjected to non-stationary excitations, as a complement for the previous subsections.

400 artificial ground motions, which are non-Gaussian, are generated, using an orthogonal expansion of a basis of random trigonometric functions. The stationary Clough-Penzien type power spectral density function (with $\omega_f = 1.3$, $\xi_f = 0.75$, $\omega_g = 13$ and $\xi_g = 0.8$) was first adopted to generate stochastic process, before a shaping function $S(t, \omega_k)$ defined how frequency contents evolve along time, as denoted in Eqs. (42)–(44). The response spectra and the evolutionary power spectral density are shown in Fig. 9.

$$S(t, \omega_k) = A(t, \omega_k) \cdot g(t) \tag{41}$$

$$A(t, \omega_k) = e^{-\eta_0 \frac{\omega_k t}{\omega_g T}} \tag{42}$$

$$g(t) = \left[\frac{t}{c}\exp\left(1 - \frac{t}{c}\right)\right]^d \tag{43}$$

wherein the ω_k is the frequency content, T is the total duration of the excitation, and the other coefficients are set as $d = 2$ $c = 8$ and $\eta_0 = 24$.

The statistical results of the responses under the 400 ground motions are shown in Fig. 10: the base moment, the top story moment and the top displacement of the primary structure are significantly reduced when compared to the UNC model, and the superiority of the VD model over the NVD model is consistent to the aforementioned findings. Additionally, the quick-decay feature of the passively-controlled models showed in the non-stationary analysis but not in the stationary analysis, as earlier peaks and shorter durations of vibration can be observed when compared with the UNC model (whose vibrations last much longer than the excitations). These differences are also shown between the VD model and the UVD model but with smaller margins. Fig. 10(d) shows how the cumulative probability curves of the base moment change along time. The dash-dot lines being far from the others indicates that the decay is quick for the passively-controlled models; however, for the UNC model, the response first evolves to be higher before slightly drops at the 30th second.

3.4. Effect of parameter uncertainties

The robustness of the structural system against the deviations of the structural parameters is preliminarily verified in the previous study; however, the uncertainties were not quantified in a systematic way. In this study, four major uncertain parameters are considered, as list in the Table 3. Monte-Carlo sampling was adopted and the frequency-domain analysis was carried out subsequently, leading to the results shown in Figs. 11 and 12. In Fig. 11, both the cumulative probability curves and the probability density function curves indicate that the uncertainties of the structural parameters cause no change of the ranking among the models in terms of the maximum primary structure moment. The UNC model is more sensitive to the deviation of structure parameters as its probability density function is much wider distributed. The Pearson correlation values of the secondary structure mass are the biggest for both the models, as shown in the Fig. 12. This indicates that heavier secondary structure leads to worse primary structure performance,

Table 5
Information of selected waves.

Wave	Event	Station	Component
1	ChiChi 1999	CHY101	EW
2	Christchurch 2011	Pages Road Pumping Station	0
3	Hollister 1961	USGS1028	270
4	Imperial Valley 1940 (the El Centro)	USUG0117	180
5	Irpinia 1980	Sturno	0
6	L'Auila 2009	V.Aterno Colle Grilli	NS
7	Loma Prieta 1989	CSMIP 47381	90
8	San Fernando 1971	Pacoima Dam	164
9	Northridge 1994	Sylmar Olive View	360
10	Friuli 1976	Tolmezzo	0
11	Duzce 1999	Ambarli	270
12	Trinidad 1980	Rio Dell Deck near E Abutment	0
13	Victoria Mexico 1980	Chihuahua	102
14	Livermore 1980	San Ramon Eastman Kodak	180
15	Landers 1992	Twenty-nine Palms	0
16	Whittier Narrows 1987	LA Wonderland Ave	165
17	Iwate 2008	IWTH17	NS
18	Umbria 1984	Gubbio	90
19	Tabas 1978	Tabas	T
20	Kern County 1952	Santa Barbara Courthouse	132
21	Niigata 2004	NIG014	EW
22	Darfield 2010	Christchurch Resthaven	N02E
23	Friuli 1976	Conegliano	0
24	Big Bear 1992	Indio-Coachella	90
25	Hector Mine 1999	Beaumont-6th & Maple	90
26	Tottori 2000	TTR002	EW
27	Parkfield-02 2004	Bottonwillow-Hwy 58 & W	90
28	Niigata 2004	NIG003	EW

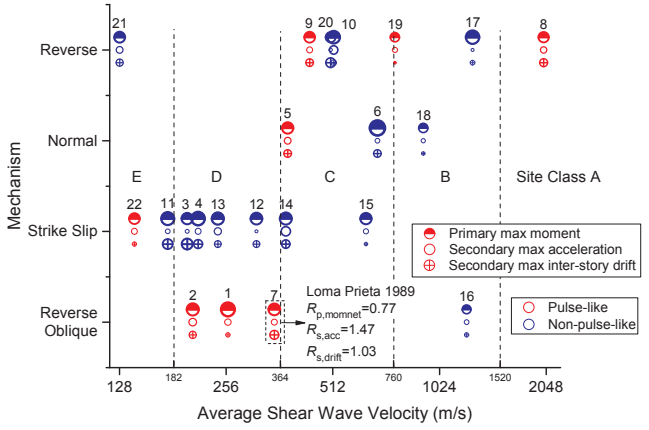

Fig. 16. Site classes and mechanisms of selected waves (diameters of dots representing the reciprocals of response ratios of the VD model).

given the fact that $R_m = 2$ is a relatively large mass ratio. It is consistent with the common perception that suspended segment acts like both the damper and the source of a driving force. However, the smaller value in the VD model suggests that with better designed secondary structure, such driving force input can be reduced. Stiffer primary structure also leads to larger moment (but smaller displacement) in primary structure. Despite the small Pearson correlation values, the deviations of the damping coefficient scalar and the inter-story stiffness scalar actually affect the MMSMP, but in a smooth way; it can be observed that the VD model show a stronger trend and thus is slightly less robust against the deviation of these two parameters.

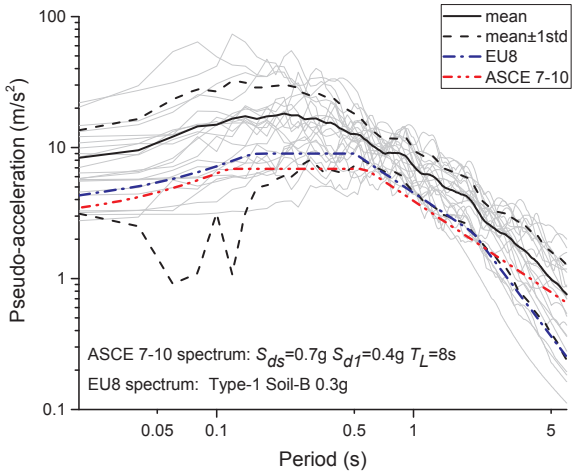

Fig. 17. Response spectra of selected waves along with code spectra.

4. Multi-objective optimization analysis

4.1. Selection of essential objectives

We carried out multi-objective optimizations to analyze the interrelationship among different responses in both parts of the structural system, before we selected fewer essential objectives as representatives.

Initially, five objectives were targeted in the multi-objective optimization to identify the dependences among them, including MMSMP, MMSDS, total damping coefficient $\sum_i c_i$, MMSAS and MMSUR, as defined in Eqs. (35)–(38). As shown in Fig. 13, sufficient crossings exist between the average-normalized values within the Pareto set of the D2-VD-AMP low model, indicating good representativeness of these objectives. However, further selection can be made according to the homogenized trade-off index proposed by Unal, Warn and Simpson [37], which can be regarded as the ratio of the crossing number to the maximum possible crossing number between two specific objectives among the Pareto solutions. Their dependence level is negatively correlated to the trade-off index. As observed in Table 4, MMSUR is strongly dependent on MMSDS, and MMSAS is moderately dependent on MMSMP (the latter being consistent with observations in [3,11]). Hence, they are removed from the set of objectives.

Thus, the set of three essential objectives can be divided into two dual-objective subsets, and we carried out the analysis in these two groups respectively in order to avoid the computationally demanding and graphically complicated tri-objective optimizations.

4.2. Dual-objective optimization analysis

The MMSMP-$\sum_i c_i$ Pareto fronts hardly cross and they are well separated, as shown in Fig. 14, indicating a clear hierarchy from this perspective. Overall, no extra dampers are required when considering vertical distributions for further optimization. The VD model gains predominance, while it has much weaker performances in terms of the non-objective responses (MMSDS and MMSAS), where the VD-AMP low/high models show comprehensive performances resulting from lower levels of vertical irregularities. The constraint on the total damping coefficient acts similarly to all response quantities and to all models, showing nearly the same trends.

The aforementioned "parameters' paths to optimum" issue can be best observed in the VD-LEV model. As only 3 discrete values are available for elements in distribution vectors, a smooth change along the whole front is not possible, and conversion points emerge in not only the Pareto front but also the projections.

The MMSMP-MMSDS Pareto fronts also hardly cross, as shown in Fig. 15, but they are not well-separated except for that of the NVD

Table 6
Information of chosen models in time history analysis.

Model	MMSMP (10^{13} kN^2·m^2)	MMSDS (10^{-5} m^2)	MMSUR (10^{-5} m^2)	MMSAS (10^{-2} m^2/s^4)	$\sum_i c_i$ (10^4 kN·s/m)
D2-NVD	19.89	5.99	17.63	1.75	5.12
D2-VD-AMP low	15.58	3.22	10.72	1.04	3.62
D2-VD-AMP high	13.90	8.78	13.09	2.92	0.87
D2-VD-LEV	10.24	18.89	19.38	5.61	1.37
D2-VD	9.66	18.34	18.99	5.35	1.03

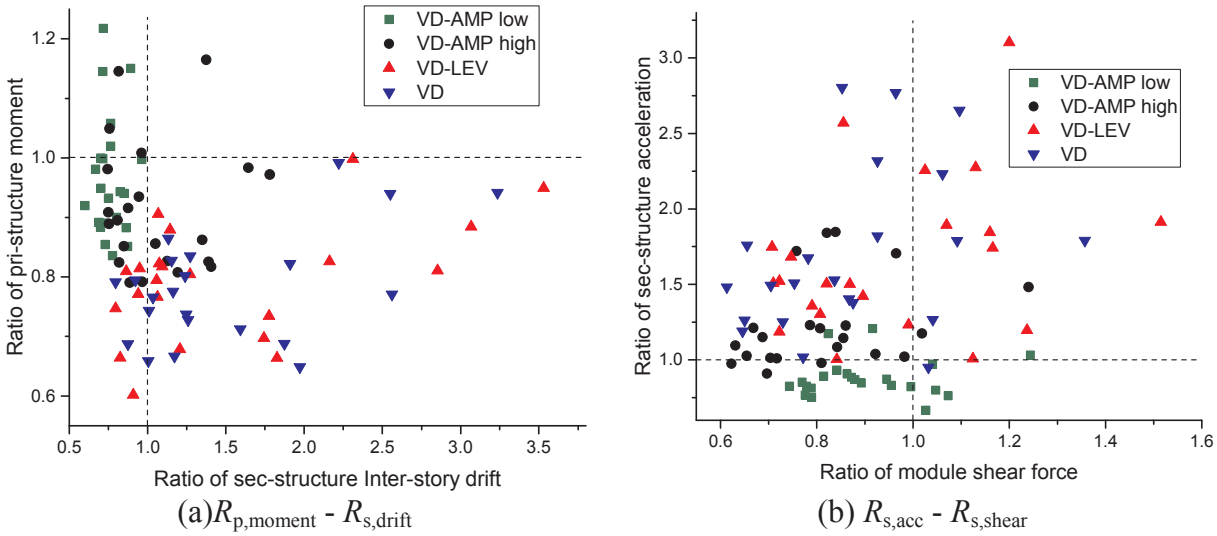

Fig. 18. Projections of time-history responses.

model. This indicates that when sufficient secondary drift is not allowed, vertical irregularity cannot enhance the control of the primary response but it still reduces demand for dampers at the expense of larger acceleration. The AMP models show trends that are nearly the opposite to those of the LEV and VD models, when MMSDS reduces, as marked by the grey arrows. Dissipation of the optimum AMP models is vertically well-distributed and not concentrated as shown in Fig. 4(b); when stiffness increases, inter-story dampers are transferred to the pri-sec structures interfaces so that over-binding of intermediate stories is avoided and the interface dissipation is enhanced. Stiffness and damping at interfaces also increase for the LEV and VD models, but it leads to larger input to the core tube and detuning effect. As a compensation, the binding of modules switches to lower stories in order to soften its tide to the core, leading to lower sensitivity to the rotation of the top and thus reduced rotation-induced accelerations. Overall, compromises can be made by which both the primary moment and the secondary drift are reduced by allowing vertical irregularities, without notable expense.

5. Time history performances

5.1. Time history performances of the linear models optimized in frequency domain

The first twenty-two strong ground motions listed in Table 5 are selected and shown in Fig. 16, covering a wide range of mechanisms, average shear wave velocities and pulse-like features. Peak ground velocities are scaled to 70 cm/s in order to match the code spectra as shown in Fig. 17. The calculation models' parameters are chosen not far from the right end on the MMSDS-$\sum_i c_i$ Pareto fronts, and their mean square responses in frequency domain and the total damping coefficients are shown in Table 6. The inherent damping of the structures is in Rayleigh form, corresponding to 1% damping ratio at the first secondary-response-dominated mode and the first primary-response-dominated mode.

For convenient comparisons, we defined response ratios as

$$R_i^j = \frac{r_i^j}{r_i^{NVD}} \tag{44}$$

where R_i^j is the response ratio of ith response in the jth model, r_i^j is the time-history maximum of the ith response in the jth model, and r_i^{NVD} is that of the NVD model.

The diameters of dots in Fig. 16 represent the reciprocals of response ratios of the VD model $1/R_i^{VD}$, showing a highly steady advantage in the primary moment against the varying of wave features and slightly less steady performances of the secondary structure on the whole figure. Such a pattern suggests that the optimization criteria are effective over a broad range of site conditions and potential seismic events.

Projections of time-history responses are plotted in Fig. 18, with the response ratios being coordinate values. The X and Y axes of Fig. 18(a) are response ratios of primary moment and secondary drift and those of Fig. 18(b) are response ratios of secondary acceleration and module shear force. Distributions and clustering can be clearly observed, that the VD and VD-LEV models considerably and steadily reduce primary responses at the expense of more scattered and larger secondary responses while the VD-AMP models exhibit mild but more comprehensive reductions. Such results match those of the frequency domain analyses.

Fig. 19 shows the envelopes of time-history maximum responses. By optimizing vertical distribution, reductions of moments in the primary structure can be observed not only at the base but also along the height. Moments in the top story are noticeable as indicated in Section 3.2.1, yet they are reduced compared with the NVD model. Inter-story drifts of the secondary structure concentrate more or less on the interfaces between the primary and secondary structures, but drifts in other stories are not to be neglected since minor concentrations exist, for instance, on the fifth floor. The VD and VD-LEV models show obvious

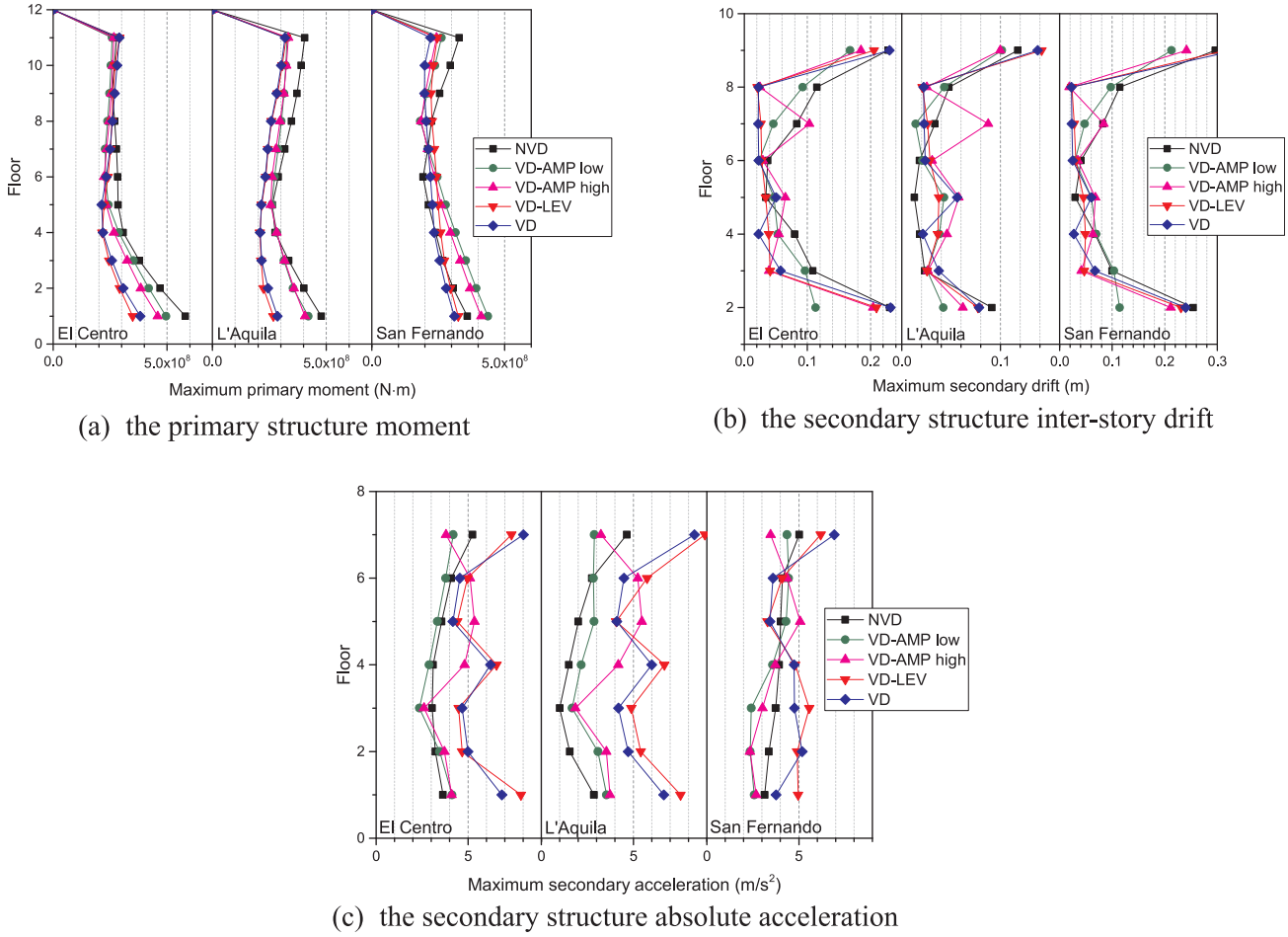

(a) the primary structure moment

(b) the secondary structure inter-story drift

(c) the secondary structure absolute acceleration

Fig. 19. Envelopes of time-history maximum responses.

concentrations as they bind the upper stories of the secondary structure. These two models also experience higher secondary structure accelerations along the height, with rotation-related patterns, while the VD-AMP low and NVD models have much lower and evenly distributed secondary accelerations.

Fig. 20 shows the time-histories of base moments of the primary structure and absolute acceleration of the secondary structure, under the El Centro wave. In terms of base moments, all controlled models show the features of lowered peaks and quick decay, with peak values varying from 21% to 33% of that of the UNC. When compared to the NVD model, the VD-LEV and VD models reduce the peak values to about 60%; the VD-AMP low model has only a slight reduction in base moment but a moderate reduction in secondary acceleration. Fourier amplitudes of base and top moments of the primary structure are also plotted, showing great accordance to the trend of the transfer functions, thus validating the optimization analyses at least for wide-band inputs such as the El Centro wave. The top moments reach similar Fourier amplitudes of the base moments around the third peak of transfer functions, but they are much less dominated by the lower frequency peaks. Fig. 21 shows deformed shapes in different instants under the Hollister wave, revealing some response characteristics of each model.

5.2. Time domain optimization and verification

The previous optimizations are all in frequency domain. As shown in Section 3.3, some main features of the modularized suspended building structure can not be captured (for instance, quick decay of vibration). As a necessary complement, time-domain optimization is carried out using the last 6 ground motions listed in Table 5 (all belong to the Site Class D according to ASCE7-10). Another 6 ground motions (wave #1 to #4, and wave #12 to #13), which also belong to the Site Class D, are adopted for subsequent checking. The motions for optimization are matched to the corresponding design spectrum while the others are scaled to PGV = 0.7 m/s.

The set-up of the optimization is mostly similar to the frequency-domain optimization, except that the objective function O is the mean square value of the root-mean-squares of the primary structure base moment in the 6 ground motions.

$$O = \frac{1}{6}\cdot\sum_{i=1}^{6}\left(\frac{1}{t_{d,i}}\cdot\int_0^{t_{d,i}} M_{base}^2(t)dt\right) \tag{45}$$

Wherein the $t_{d,i}$ denotes the duration time of the ith motion and M_{base} denotes the base moment of the primary structure.

Models optimized in time domain are named with an additional "–t"; those with nonlinear viscous damper has another –x, wherein x denotes the damping exponent; for instance, NVD-t-0.5 represents the NVD model optimized in time domain and implemented by viscous dampers with a 0.5 damping exponent.

The optimized modules parameters show a high level of resemblance of those optimized in frequency domain, as can be observed in Table 7, where the stiffness scalar R_k stay almost unchanged, indicating that the tuning effect is also the key in reducing time-history responses. The damping coefficient scalar R_c shows the same merit, except for those with damping exponents lower than 1. The vertical distribution vectors also exhibit very similar patterns, as shown in Table 8.

Fig. 22(b) plots the scatters of response ratios (to those of the UNC model) for the models listed in Table 7, subjected to the group of 6 ground motions for checking. Highly resemble patterns, between

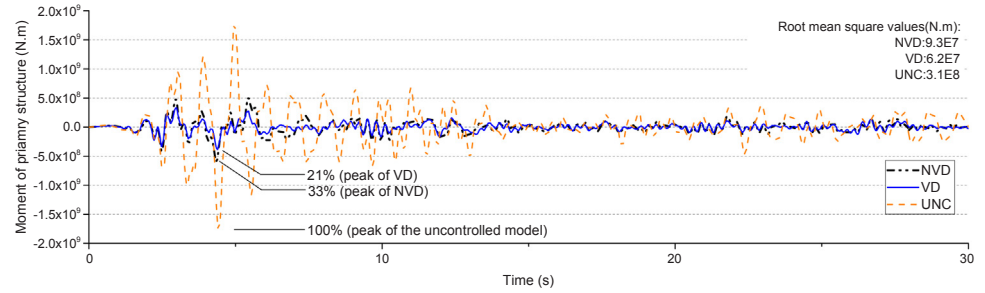

(a) base moment of the primary structure (with comparison to the uncontrolled model)

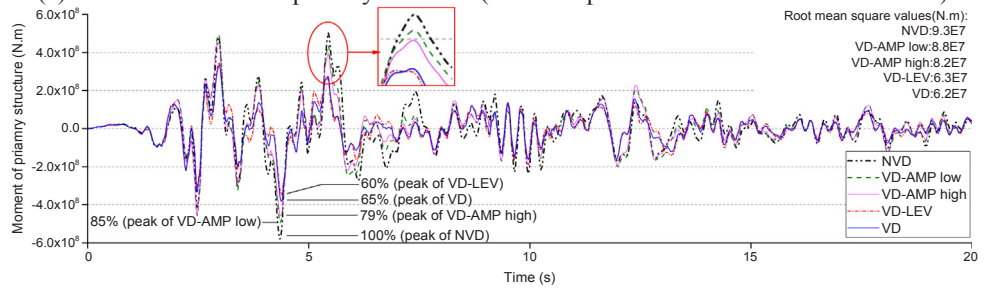

(b) base moment of the primary structure (without comparison to the uncontrolled model)

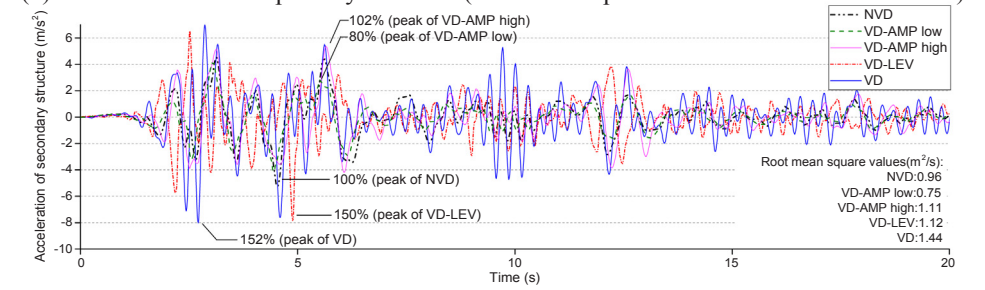

(c) absolute acceleration of the secondary structure (without comparison to the uncontrolled model)

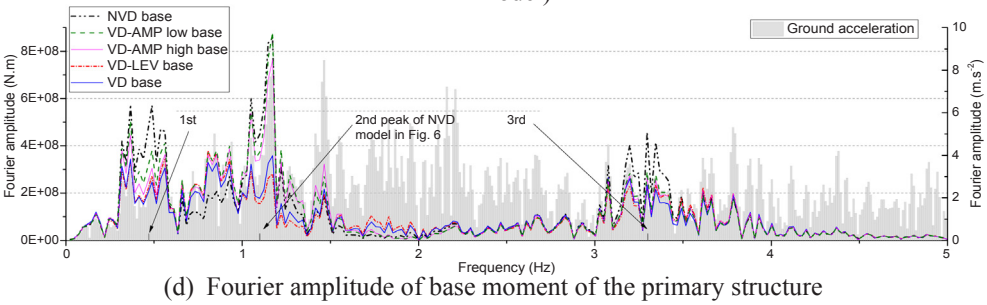

(d) Fourier amplitude of base moment of the primary structure

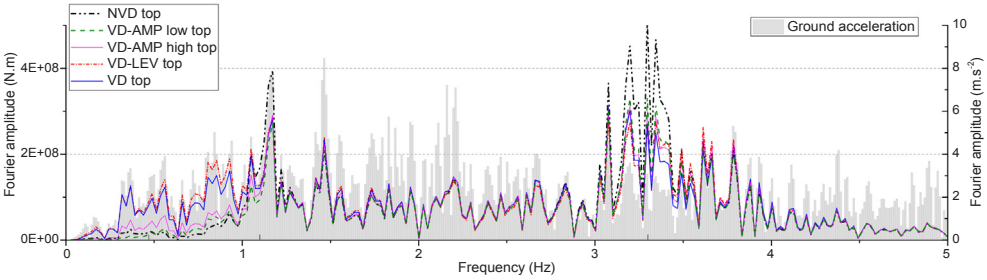

(e) Fourier amplitude of top moment of the primary structure

Fig. 20. Time-history responses and corresponding Fourier amplitudes under the El Centro wave.

models with the same configuration but their parameters optimized in different domains, are shown. The aforementioned observations prove the validity of frequency-domain optimization for the proposed modularized suspended building structures; as it takes much less time to finish one iteration, it is preferable especially in multi-objective optimization where large Pareto fronts need to be formed.

5.3. Time history performance of the nonlinear model

Under extreme cases, nonlinearity of the primary structure may develop, mainly due to the yielding of steel bars, severe cracking and spalling of the concrete. However, it is to be avoided at any cost in the level of Maximum Considered Earthquakes, because it leads to

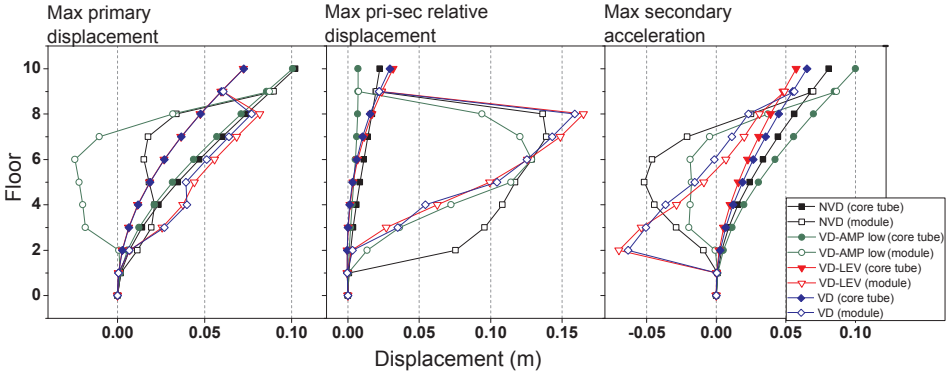

Fig. 21. Deformed shapes in different instants under the Hollister wave.

Table 7
Comparison between the model parameters optimized in different domains: part (a).

	NVD	NVD-t	NVD-t-0.5	NVD-t-0.3	VD-AMP low	VD-AMP low-t	VD	VD-t
R_k	35.9	38.8	32.5	30.9	98.6	71.4	23.2	20.7
R_c	426.3	475.2	76	41.6	66.9	67.5	1.1	1.2

Table 8
Comparison between the model parameters optimized in different domains: part (b).

	The vertical distribution vectors								
	Floor	1	2	3	4	5	6	7	8
VD-AMP low	$\mathbf{r}_k$	1	1	3	2.9	3	1	1	1
	$\mathbf{r}_c$	5	4.9	1.1	1.1	3.7	4.7	4.7	1.7
VD-AMP low-t	$\mathbf{r}_k$	1.9	1.6	2.7	2.6	2.6	1.2	1.2	2
	$\mathbf{r}_c$	5	4.8	2.6	2.4	4.2	3.6	4.6	1.4
VD	$\mathbf{r}_k$	1	21	88	23	100	100	65	1
	$\mathbf{r}_c$	289.8	1	1	217.6	1	1	1	1
VD-t	$\mathbf{r}_k$	1	19.2	61.6	43.4	100	100	100	1
	$\mathbf{r}_c$	211.9	1	1	450	1	1	1	1

demolition or even collapse of the whole building.

The nonlinearBeamColumn element of OpenSees, which is a prismatic element with spreading of plasticity and Gauss-Lobatto quadrature integration rule, is adopted in modeling the elasto-plasticity of the primary structure. Other details of the element and the section are shown in Fig. 1. This modal is calibrated so that all modal frequencies and mode shapes are almost the same as the optimized linear model.

The vibration control effect provided by modular suspended structure becomes less obvious when elasto-plasticity develops, especially for the time-history-peak of the base moment, as shown in Fig. 23(a); in this figure the VD model shows no advantage over the NVD model, because the develop of the plasticity totally undermines the multi-mode tuning features of the VD model. In Fig. 23(b) and (c), it can be observed that the advantage of VD model becomes less obvious as the intensity of the ground motion increases and the nonlinearity develops. However, in this case, the UNC model experiences a large residual displacement while the NVD module experiences a small one, but the VD module shows almost no sign of residual displacement. Fig. 23(d) shows that when the nonlinearity is developed in all models, the VD model has no obvious advantage over the NVD model in terms of the primary structure displacement, though both the VD and the NVD model outperform the UNC model. However, the NVD model still exhibited smaller acceleration in modules when compared with those of the other two.

6. Discussion

Drastic irregularities with minor blocks and concentrated responses exist in the optimized secondary structures, indicating that the features of modularization (protection and clear inter-story relationships) are well harnessed. As a result, the seismic control performance is further improved, compared with the previous research [14]. At least the first three peaks in the transfer function of the primary structure moment

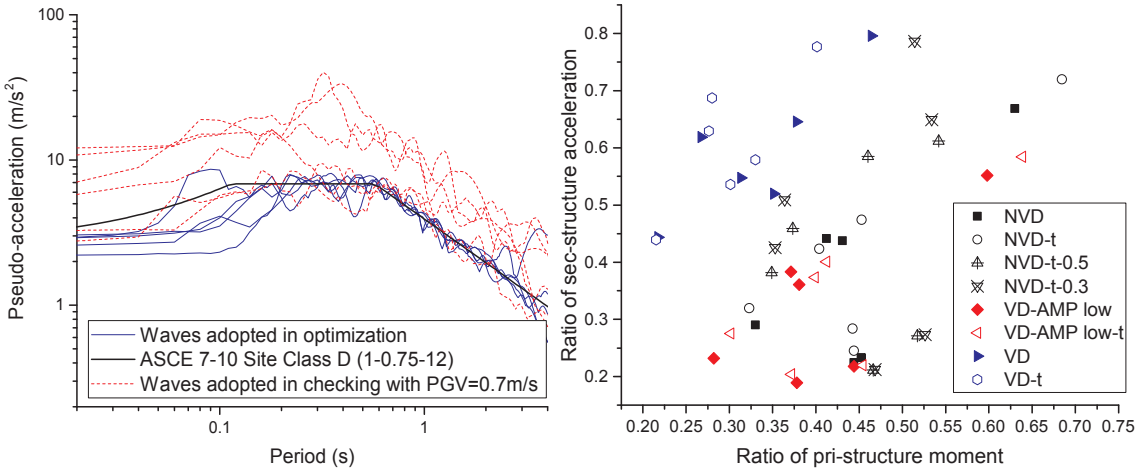

(a) The ground motions spectra (b) Response ratio scatter plot

Fig. 22. The response spectra for ground motions (adopted respectively in optimization and checking) and the response ratio.

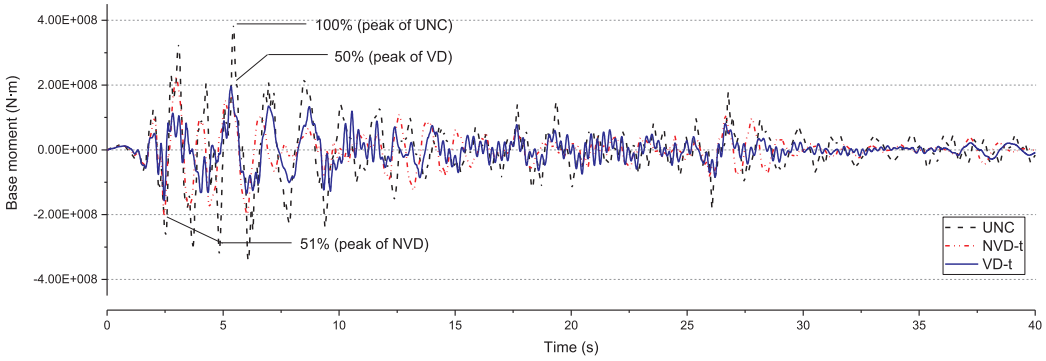

(a) Base moment of primary structure under El Centro wave with PGV=0.3m/s

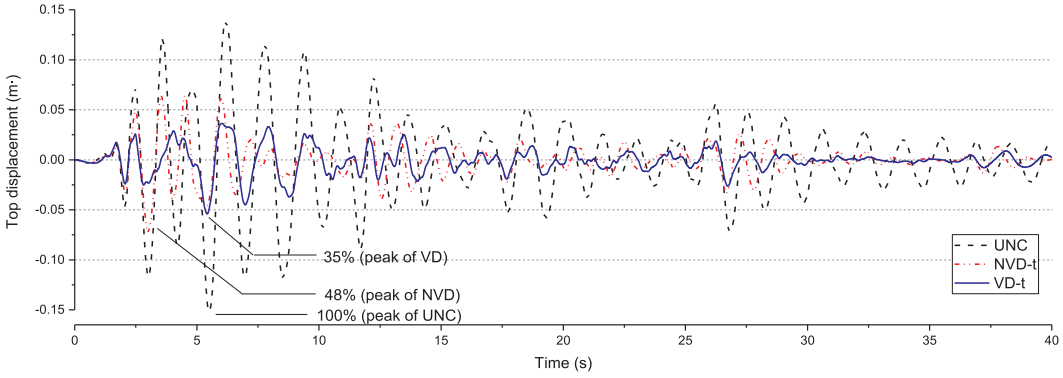

(b) Top displacement of primary structure under El Centro wave with PGV=0.3m/s

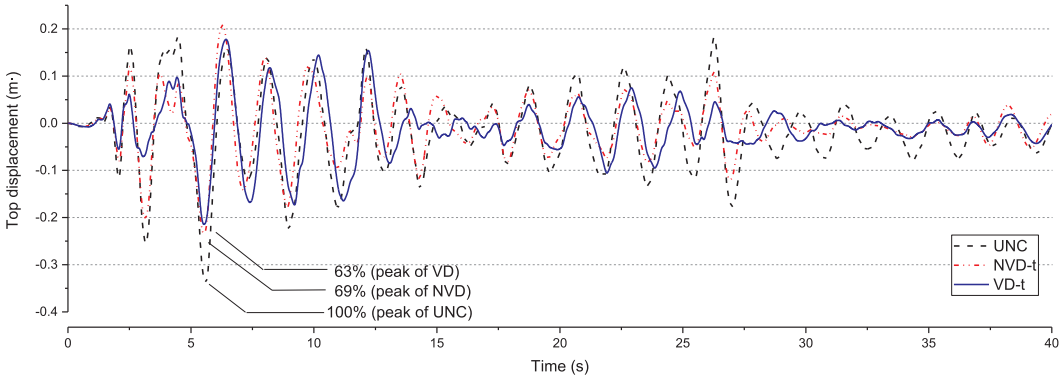

(c) Top displacement of primary structure under El Centro wave with PGV=0.7m/s

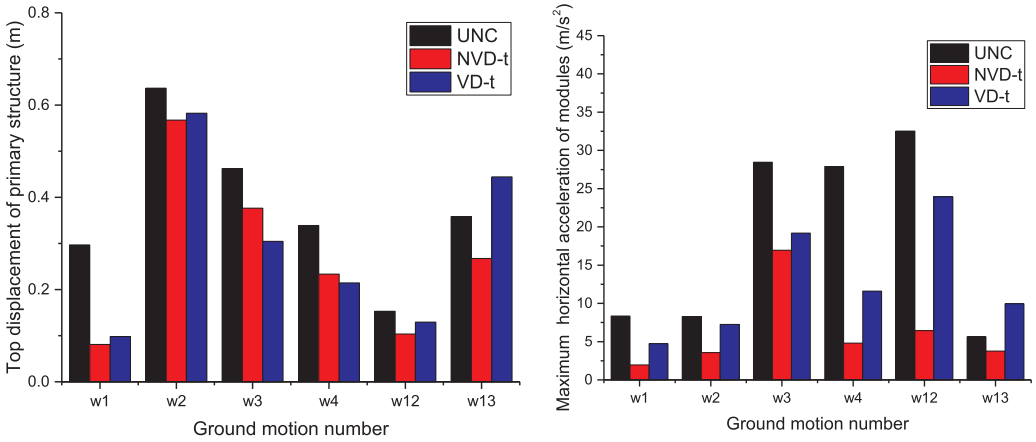

(d) Performance histograms when PGV=0.7m/s

Fig. 23. Time-history responses and performance histograms with elasto-plasticity in the primary structure.

are considerably lowered, compared to the non-vertically distributed model. Such effect can be extended to even higher modes but depends on whether the optimization drives it to. Primary-structure-oriented optimum requires a high level of vertical irregularities while mild irregularities bring about moderate but comprehensive improvement. Overall, such distribution for a large-scale secondary structure is analysed for the first time in this study and shows promising potential in seismic vibration control.

The advantages originate from better dissipation brought by satisfactory tuning effects between the primary and the secondary structures, as the irregularities allow flexible spacing of major modes and the optimization makes them well-spaced in frequency domain. The optimized models tend to concentrate dampers in the low stiffness stories, leading to higher dissipating efficiency without excessive demand for dampers, but they are not over-concentrated so that multiple major modes can be well damped.

We have carried out mainly elastic analyses, as the secondary structure experiences little damage and the primary structure responses are attenuated. Besides, as the core tube is mostly strong to guarantee vertical redundancy and its robustness against the varying of parameters is revealed, the results are valid at least for moderate earthquakes. However, a preliminary nonlinear analysis is carried out to capture the basic features, but without considering more of the subsequent practical issues such as ponding between modules and the core-tube, and over-stroke of dampers. Those are within the scope of a future study.

The system is recommended to be applied in 10–25-story residential or office buildings which are amenable to modularization techniques. Within this height range, single suspended segment is adequate and core-tube is an economic form for the primary structure. A higher suspended segment may experience a better multi-mode control effect; this factor is worth future investigation. Width should also be kept within a suitable range in order to avoid the unpleasant coupling of the truss rotation and the vertical inertia of modules.

7. Conclusion

We further explored the seismic control potential of modularized suspended structure recently proposed by the authors, by optimizing the vertical distributions of the secondary structure parameters. Several strategies are considered by setting different constraints on distribution vectors. Single/multiple objective optimizations and time-history analysis are carried out to comprehensively study the improvement of seismic performances. Non-stationary excitations and parameters uncertainties are also analysed, as necessary complements for the simplified optimization model.

1. At the primary structure-oriented optimums, unconstraint vertical distribution reduces the primary structure responses to a low percentage at the expense of moderately increased secondary responses, especially accelerations. To the contrary, the distribution with a constraint on the differences among elements' amplitudes mildly reduces all responses.
2. The distribution with limited scattered levels of allowable values shows an effect similar to that of the unconstraint one, but requires many more dampers.
3. The multi-mode control effect is improved and the better tuning between primary and the secondary structures is the key mechanism. The VD model has its secondary structure deformation concentrated in a different combination of stories in each of the major modes, while the majority of secondary structure sways to the opposite direction as those of the primary structure, providing satisfactory dynamic stiffness and dissipation.
4. The peak of the damping vector tends to occur at the trough of the stiffness vector but without excessive concentration, leading to higher dissipation efficiency for several modes. This also helps prevent excessively increased inter-story drift in the secondary structure.
5. The analysis under the non-stationary excitations proves the inherent features of quicker decay of the modularized suspended structure with the optimized vertical distribution of parameters, as also suggested by the large negative real component of the eigenvalue of the major complex modes.
6. The system shows satisfactory robustness against the deviation of parameters, so does the benefit of optimum vertical distributions. While a heavier secondary structure may undermine the control performance, the model with optimized vertical distributed parameters shows a lower sensitivity to the variation of secondary mass.

Overall, vertical distributions of the secondary structure parameters considerably improve the performance of modularized suspended structure and they will not cause damage even under excessive and concentrated inter-story drift in the secondary structure, due to the protection effect of the suspended discrete modules.

Acknowledgement

This work was supported by the National Key Research and Development Program of China (2016YFC0701400); the Cheung Kong Scholars Program; the National Science Fund for Distinguished Young Scholars (51525801); the Fundamental Research Funds for the Central Universities (2242017k30002), the Natural Science Foundation of Jiangsu Province (BK20170680) and Priority Academic Program Development of Jiangsu Higher Education Institutions (1105007002).

Appendix A. Supplementary material

Supplementary data to this article can be found online at https://doi.org/10.1016/j.engstruct.2018.12.099.

References

[1] Goodno BJ, Gere JM. Earthquake behavior of suspended-floor buildings. J Struct Div-ASCE 1976;102(5):973–92.
[2] Mezzi M, Parducci A, Marioni A. Aseismic suspended building based on energy dissipation. 10th European conference on earthquake engineering. Vienna: Balkema; 1994.
[3] Feng MQ, Mita A. Vibration control of tall buildings using mega subconfiguration. J Eng Mech-ASCE 1995;121(10):1082–8.
[4] Villaverde R. Roof isolation system to reduce the seismic response of buildings: a preliminary assessment. Earthq Spect 1998;14(3):521–32.
[5] Zhang YH, Liang QZ. Asynchronous driving principle and its application to vibration control. Earthq Eng Struct Dyn 2000;29(2):259–70.
[6] Lan Z, et al. An experimental study on seismic responses of multifunctional vibration-absorption reinforced concrete megaframe structures. Earthquake Eng Struct Dyn 2004;33(1):1–14.
[7] Wang C, Lü Z, Tu Y. Dynamic responses of core-tubes with semi-flexible suspension systems linked by viscoelastic dampers under earthquake excitation. Adv Struct Eng 2011;14(5):801–13.
[8] Nakamura Y, et al. Development of the core-suspended isolation system. Earthq Eng Struct Dyn 2011;40(4):429–47.
[9] Reggio A, De Angelis M. Optimal energy-based seismic design of non-conventional Tuned Mass Damper (TMD) implemented via inter-story isolation. Earthq Eng Struct Dyn 2015;44(10):1623–42.
[10] Mahmoud H, Chulahwat A. Response of building systems with suspended floor slabs under dynamic excitations. Eng Struct 2015;104:155–73.
[11] Xiang P, Nishitani A. Optimum design of tuned mass damper floor system integrated into bending-shear type building based on $H\infty$, H_2, and stability maximization criteria. Struct Contr Health Monit 2015;22(6):919–38.
[12] Tan P, et al. Experimental investigation of mega-sub isolation structure. Struct Des Tall Special Build 2017;26(16):e1360.
[13] Ryan KL, Earl CL. Analysis and design of inter-story isolation systems with nonlinear devices. J Earthq Eng 2010;14(7):1044–62.
[14] Ye Z, Wu G. Optimal lateral aseismic performance analysis of mega-substructure system with modularized secondary structures. Struct Des Tall Special Build 2017;26(17).
[15] De Angelis M, Perno S, Reggio A. Dynamic response and optimal design of structures with large mass ratio TMD. Earthq Eng Struct Dyn 2012;41(1):41–60.
[16] Wittfoht H, Cretu G. The 'Bell-Building': a new type of earthquake resistant structure. Proceedings of the 5th Canadian conference on earthquake engineering, Ottawa, Canada. 1987. p. 593–7.

[17] Chai W. Mega-sub control of high-rise buildings. Irvine: University of California, Irvine; 1996.
[18] Behr RA, Belarbi A, Culp JH. Dynamic racking tests of curtain wall glass elements with in-plane and out-of-plane motions. Earthq Eng Struct Dyn 1995;24(1):1–14.
[19] Fathieh A, Mercan O. Seismic evaluation of modular steel buildings. Eng Struct 2016;122:83–92.
[20] Annan CD, Youssef MA, El Naggar MH. Experimental evaluation of the seismic performance of modular steel-braced frames. Eng Struct 2009;31(7):1435–46.
[21] Giriunas K, Sezen H, Dupaix RB. Evaluation, modeling, and analysis of shipping container building structures. Eng Struct 2012;43(5):48–57.
[22] Lawson M, Ogden R, Goodier C. Design in modular construction. Boca Raton: CRC Press; 2014.
[23] Agrawal AK, Yang JN. Optimal placement of passive dampers on seismic and wind-excited buildings using combinatorial optimization. J Intell Mater Syst Struct 1999;10(12):997–1014.
[24] Chen G, Wu J. Optimal placement of multiple tune mass dampers for seismic structures. J Struct Eng 2001;127(9):1054–62.
[25] Zuo L, Nayfeh SA. Minimax optimization of multi-degree-of-freedom tuned-mass dampers. J Sound Vib 2004;272(3–5):893–908.
[26] Negro P, Colombo A. Irregularities induced by nonstructural masonry panels in framed buildings. Eng Struct 1997;19(7):576–85.
[27] Dolsek M, Fajfar P. Soft storey effects in uniformly infilled reinforced concrete frames. J Earthq Eng 2001;5(1):1–12.
[28] Ko D, Lee H. Shaking table tests on a high-rise RC building model having torsional eccentricity in soft lower storeys. Earthq Eng Struct Dyn 2006;35(11):1425–51.
[29] Rigoni E, Poles S. NBI and MOGA-II, two complementary algorithms for multi-objective optimizations. Dagstuhl seminar proceedings. Schloss Dagstuhl-Leibniz-Zentrum für Informatik; 2005.
[30] Hoang N, Fujino Y, Warnitchai P. Optimal tuned mass damper for seismic applications and practical design formulas. Eng Struct 2008;30(3):707–15.
[31] Cheung YL, Wong WO. H2 optimization of a non-traditional dynamic vibration absorber for vibration control of structures under random force excitation. J Sound Vib 2011;330(6):1039–44.
[32] Cheng FY, Li D. Multiobjective optimization design with Pareto genetic algorithm. J Struct Eng 1997;123(9):1252–61.
[33] Marano GC, Greco R, Chiaia B. A comparison between different optimization criteria for tuned mass dampers design. J Sound Vib 2010;329(23):4880–90.
[34] Xie Y, Zhang J. Optimal design of seismic protective devices for highway bridges using performance-based methodology and multiobjective genetic optimization. J Bridge Eng 2016;22(3):04016129.
[35] Tsuji M, Nakamura T. Optimum viscous dampers for stiffness design of shear buildings. Struct Des Tall Build 1996;5(3):217–34.
[36] Takewaki I. Displacement–acceleration control via stiffness–damping collaboration. Earthq Eng Struct Dyn 1999;28(12):1567–85.
[37] Unal M, Warn GP, Simpson TW. Quantifying the shape of a pareto front in support of many-objective trade space exploration. ASME 2016 international design engineering technical conferences and computers and information in engineering conference. American Society of Mechanical Engineers; 2016.